A Dosimetric Evaluation of MiniPIX Performance Using In-situ and Simulated Environments

---

A Senior Honors Thesis Presented to

the Faculty of the Department of Physics

University of Houston

In Partial Fulfillment

of the Requirements for the Degree

Bachelor of Science

By

Reed Bronson Masek

May 2020

A Dosimetric Evaluation of MiniPIX Performance Using In-situ and Simulated Environments

---

Reed Bronson Masek

APPROVED:

Dr. Andrew Renshaw

Department of Physics, Committee Chair

Dr. Stuart George

Department of Physics, Committee Co-Chair

Dr. Donna Stokes

Department of Physics, Committee Reader

Dr. Dan Wells, Dean

College of Natural Sciences and Mathematics

ACKNOWLEDGEMENTS

I want to thank Dr. Andrew Renshaw for spending the majority of my undergraduate career with me. When I first began looking for research opportunities, I had no idea what I was looking for or what I was wanting to do as a Physics student. After I reached out to him, Dr. Renshaw invited me to spectate his undergraduate research group which opened up the numerous opportunities and experiences which followed.

Additionally, thanks go to Dr. Donna Stokes and Dr. Oomman Varghese who were fabulous lecturers and mentors. Although they may not realize it, they both helped to push and encourage me as well as many other undergraduates.

I also would like to acknowledge Max Renschler at the Karlsruher Institut für Technologie in Karlsruhe, Germany for allowing me to spend a summer working with him on his Ph.D research. My time with him reinforced my interests in Physics and inspired me to continue on a journey towards a Ph.D of my own.

I cannot forget the countless hours spent with my fellow Physics students, and the lasting and fulfilling friendships with many of them.

Of course, all the people I met during my years in the HASP program are to thank. They were mentors and teachers when they needed to be and inspired me to push myself, but ultimately they were my friends with whom I spent countless hours with during my time as an undergraduate.

Of course, this journey would not have begun without the persistent and continued support of my parents during my studies. They constantly provided encouragement and helped me get to the finish line.

A Dosimetric Evaluation of MiniPIX Performance Using In-situ and Simulated Environments

---

An Abstract of Senior Honors Thesis

Presented to

the Faculty of the Department of Physics

University of Houston

In Partial Fulfillment

of the Requirements for the Degree

Bachelor of Science

By

Reed Bronson Masek

May 2020

ABSTRACT

Space weather is becoming increasingly relevant as human activity in space and around grows. Primary contributors to this space radiation are galactic cosmic rays (GCRs) which continue to mystify scientists with their high energies and unknown origins. Despite the unknowns, active monitoring of the radiation environment beyond the Earth's surface is important for the safety of commercial airlines and astronauts. This thesis examines the use of a MiniPIX camera as a relatively low-cost, portable radiation dosimeter used on-board high altitude balloon flights under the High Altitude Student Platform (HASP). The MiniPIX was housed within a miniature container designed to replicate the structure of the International Space Station (ISS). The goal of this construction is to model a complex and exotic environment, such as the ISS, using a simplified representation in attempt to reduce the high dependence of simulations for monitoring the dose received by human on commercial flights or in space by generalizing this methodology to other applications. Its performance is compared to simulations executed by the FLUKA transport code which strive to replicate the atmospheric environment and GCR sources during the HASP missions. The use of the simulations in this context is to validate the configuration flown on the balloon. The results from the simulations are not directly comparable to those from the balloon, but characteristic features within the simulated data are present. Lastly, results from experiments and simulations performed by others are examined and compared to the results from the HASP mission and the simulations performed in this study.

TABLE OF CONTENTS

ACKNOWLEDGEMENTS . . . iii
ABSTRACT . . . v
LIST OF FIGURES . . . ix
LIST OF TABLES . . . x

1 INTRODUCTION **1**
1.1 Space Weather . . . 1
1.2 Secondary Cosmic Rays . . . 3
1.3 Monitoring Radiation . . . 5
1.4 Active Monitoring of the High Altitude Radiation Environment . . . 8

2 THE MINIPIX PIXEL DETECTOR **9**
2.1 Semiconductor-Based Pixel Detectors . . . 9
2.2 The Medipix and Timepix Chips . . . 11
2.2.1 Timepix Signal Processing . . . 11
2.3 MiniPIX Device Characteristics . . . 12
2.4 Operational Parameters . . . 14
2.4.1 Calibration . . . 15
2.5 Medipix Output . . . 17
2.5.1 Particle Morphology . . . 17

3 ATMOSPHERIC DOSIMETRY WITH A MINIPIX DEVICE **21**
3.1 A Typical HASP Mission . . . 22
3.2 Development of a Real-Time Dosimeter . . . 23
3.2.1 Hardware . . . 23
3.2.2 Analysis Procedure . . . 24
3.3 Mock-up International Space Station - MISS . . . 25
3.3.1 Construction and Materials . . . 26
3.3.2 Inaccuracies in the MISS Construction . . . 28
3.3.3 Altitude Calculations . . . 30
3.4 Results from MISS . . . 31
3.4.1 Dosimetry Measurements . . . 31
3.4.2 Comparison to Previous Missions . . . 36
3.5 Conclusions on MISS . . . 38
3.5.1 Contributions of the Author . . . 38
3.5.2 Future Missions . . . 38

4 THE FLUKA MULTI-PARTICLE TRANSPORT CODE **41**
4.1 A Brief History of FLUKA 41
4.2 Flair 43
4.3 The Simulation Environment 43
4.3.1 Preparing and Running a Simulation 43
4.3.2 Post-Processing 45
4.3.3 GCR Calculations 45
4.4 Input Geometry and the Timepix 46
4.4.1 The Earth Model 46
4.4.2 The MISS Model 48
4.4.3 Simulation Benchmarking 50
4.5 Simulation Results 51
4.6 Discussion and Works Performed by Others 53
4.7 Conclusions on the FLUKA Study 55

5 CONCLUSIONS **57**
5.1 Future Work 58

Appendices **61**

A MISS Detailed Specifications **61**

B Medipix Metadata **63**

BIBLIOGRAPHY **65**

LIST OF FIGURES

1.1.1 A graphical presentation of the cosmic ray spectrum using the results of various experiments around the world. This plot was borrowed from Ref. [1]. 3
1.1.2 A plot showing the correlation between the number of sunspots and the dose rate on the lunar surface over a few decades. This plot is reproduced from Ref. [2]. . . . 4
1.2.1 A breakdown of contribution to dose from secondary particles as a function of altitude. Commercial airline flights are typically in the 10 km to 13 km range; note the high presence of neutrons. This plot is sourced from Ref. [3]. 6

2.3.1 Image of the MiniPIX plugged into the USB port of a computer. 12
2.3.2 Examples of the temperature dependence of Timepix pixels. Both data frames feature incorrect data. Note the energy scale below the images. 14
2.4.1 An example of two intersecting tracks near the bottom left corner of the frame marked by the green circle. 16
2.5.1 A table showing the different morphological classes, their criteria, and an example of a cluster as recorded by the pixel sensor. This graphic is sourced from Ref. [4]. . . 18
2.5.2 Q_{60} as defined in ICRP Publication 60. 19

3.2.1 An example from of a bounding box around a particle track (the dotted black box surrounding the particle track), and the fit line (the solid black line along the particle track). This visual is borrowed from Ref. [4]. 25
3.3.1 Layout of the 2019 UH HASP payload showing the location of MISS. The only obstruction between the MiniPIX and the atmosphere is the MISS structure. 26
3.3.2 ISS shielding used by different space agencies as given by Ref. [5]. The number preceding the words “Kevlar” or “Nextel” refer to the number of fabric layers. . . . 27
3.3.3 Cross section of the layers used to construct MISS. All dimensions are in millimeters. 28
3.3.4 Rendering of the final MISS concept. 29
3.4.1 Plots of absorbed dose and particle counts recorded by MISS throughout the balloon flight. The Regener-Pfotzer maximum is clearly visible in the count rate and dose rate. 32
3.4.2 LET histograms for each particle cluster type. Both figures show the same data but with different scales for the vertical axis. 35
3.4.3 LET density distribution by cluster type. 35
3.4.4 MiniPIX data frame showing a 109 nGy event recorded during flight. 36
3.4.5 MiniPIX dose rate from the 2017 and 2018 UH HASP missions alongside the LET histogram from the 2018 data. The results from MISS are reproduced for comparison. 37

4.4.1 Image depicting MISS within FLUKA. The layers, as previously defined, are clearly shown along with the Timepix sensor in the inner-most region. The white regions, which depict empty space, were given the same gaseous composition as the atmospheric layer within MISS resided for each particular altitude. 49
4.4.2 Example of a plot featuring `USRBIN` data from an example simulation in which a proton beam was shot at a thin silicon target. 50
4.4.3 FLUKA benchmark results using its standard GCR models at solar minimum. . . . 51
4.5.1 Dose measurements made by the FLUKA simulations. The results were put into 3 km wide bins similar to the dose measurements made by MISS during the balloon flight. 52
4.5.2 Fluences obtained from the simulation configuration. These are the results from one simulation run, but all 36 runs shared similar results for these variables. 53
4.6.1 Results from the RaD-X campaign prior to the application of filtering techniques, as presented in Ref. [6]. The TID results are shown in green. 55

A.0.1A detailed view of the front panel construction for MISS. 61
A.0.2A detailed front view of MISS with the front plate removed. 62

LIST OF TABLES

3.1 Definition for the first four atmospheric layers and their respective constants. 31

Chapter 1

Introduction

1.1 Space Weather

Weather in space is a topic of contemporary relevance as human activity in space increases with the growth of both government-based and privatized space programs. Examples of this growth can be seen in the launch of NASA's Artemis program [7], the opening of the International Space Station (ISS) in 1998 and its continuous occupation for the last 18 years [8], and the various technological advances in the business sector for developing vehicles made by companies such as Space-X. This persistent and growing human presence in space calls for careful monitoring of astronauts' exposure to radiation as well as a standard with which that exposure can be measured.

Primary cosmic rays is a term that describes a general group of high-energy, charged particles consisting of partially ionized or fully ionized atoms. Hydrogen and helium nuclei constitute the majority of the primary cosmic ray spectrum, but heavy atoms such as iron and uranium can be detected in trace amounts [9]. Galactic cosmic rays (GCRs) are a subset of primary cosmic rays with their distinguishing property being that they have galactic and extra-galactic origins. A general understanding of their production and acceleration mechanisms is known, but a close-up and detailed look at the matter reveals that there are missing pieces [10]. For decades, GCRs have fascinated scientists with their unknown origins and extremely high energies. Tracing GCRs

is particularly difficult since their path is influenced by magnetic fields, and the exact mechanism which accelerates to most energetic of these particles to such high energies (e.g., 1×10^{20} eV) is currently unknown. High-energy gamma (γ) rays are a promising candidate for tracing the origins of GCRs. Galactic and extra-galactic magnetic fields do not deflect photons, so the origin of high energy photons can be traced as it is theorized that the high energy photons are produced alongside GCRs [1]. Furthermore, high energy photons, as well as high energy neutrinos, can be produced as secondaries in the event that a cosmic ray interacts with matter (such as interstellar gas) or the cosmic microwave background (CMB) [11] [12]. The highest measured energies are on the order of a few 100 TeV; however, this threshold is not determined by a technological limitation [12]. It is suspected that the higher energy photons are absorbed during interactions with the CMB while propagating through space [12]. Figure 1.1.1 shows the fluxes of cosmic rays for a given energy value using data gathered by various ground-based experiments. The knees and ankle that are marked in the plot have a high significance and neatly categorize the particles by their mass and origin. Most of the cosmic rays with energies up to the first knee originate from within the Milky Way galaxy. The transition from galactic to extra-galactic particles begins at the second knee and ends at the ankle, so most particles after the ankle are extra-galactic. A more detailed analysis of the causes and implications of the knees and the ankle can be found in Ref. [1] and Ref. [9].

The Earth is constantly bombarded by these high energy particles; however, the Earth's atmosphere provides substantial shielding against many of the particles. As altitude increases, the atmospheric protection is weakened, meaning people aboard aircraft, such as commercial planes receive higher doses of radiation than people on the surface. Astronauts are even more vulnerable. The Sun has a strong influence over the flux of these particles, and the variations in these fluxes correlate with the solar cycle. Figure 1.1.2 shows the trend shared between the dose rate on the lunar surface and the number of sunspots over the previous few decades.

The closest source of cosmic rays to the Earth is its own Sun. Solar flares eject solar cosmic rays, which mostly consist of protons and helium nuclei [13]. It is usual for GCR flux to vary inversely with solar activity since the magnetic fields associated with solar flares and coronal mass ejections

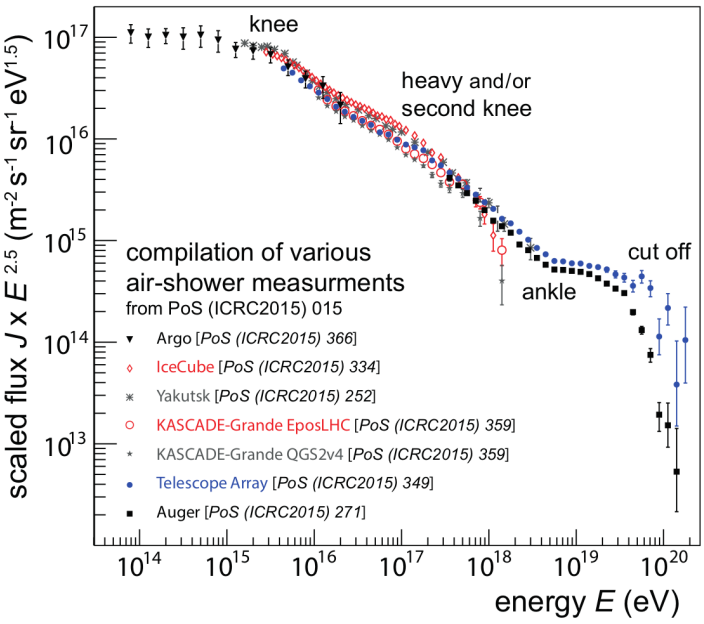

Figure 1.1.1: A graphical presentation of the cosmic ray spectrum using the results of various experiments around the world. This plot was borrowed from Ref. [1].

deflect some of the particles [14]. However, recently the solar wind has possessed "extremely low densities and magnetic field strengths," resulting in the highest GCR flux observed in the space age [2]. This unprecedented behavior exhibited by the Sun is unexpected and requires further understanding of the mechanics of the Sun. Naturally, there is a concern regarding the impact that this trend of increasing GCR flux will have on the future of humans living in space.

1.2 Secondary Cosmic Rays

The initial particles which interact with molecules in the atmosphere are referred to as primary cosmic rays. When a high energy primary cosmic ray collides with a particle in the atmosphere, secondary particles are produced which can then produce more particles in what is known as an air shower. An air shower is a cascade of particles that propagates through the atmosphere [1]. One characteristic of an air shower is the atmospheric depth, χ_{max}, which is the depth at which

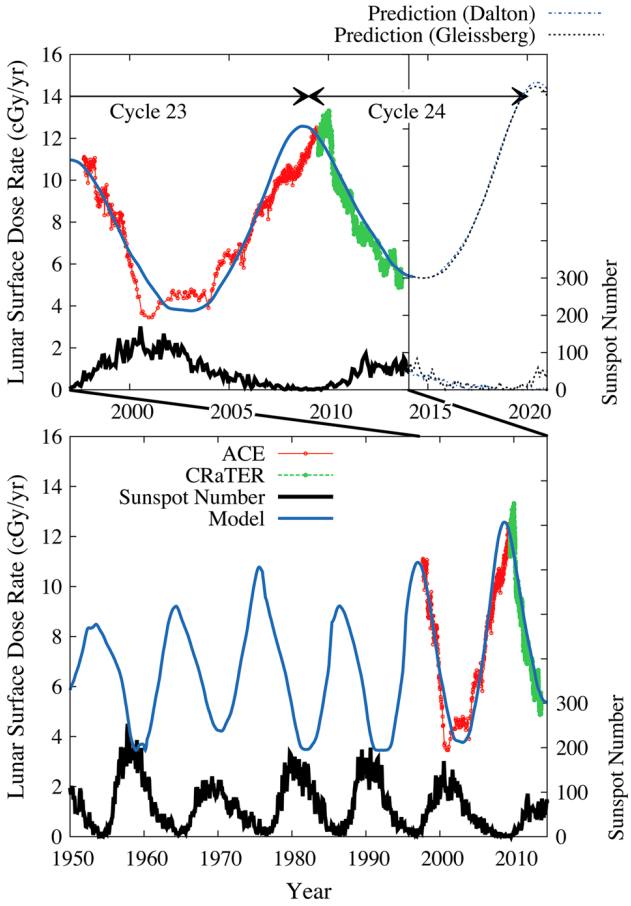

Figure 1.1.2: A plot showing the correlation between the number of sunspots and the dose rate on the lunar surface over a few decades. This plot is reproduced from Ref. [2].

the electromagnetic component of the shower is at its maximum and is related to the energy and mass of the primary particle [15]. As the energy of the primary particle increases, χ_{mas} becomes deeper. Fluorescence detector techniques can be used to measure χ_{max} and the longitudinal profile of the shower [16].

During the 1930s, Erich Regener and Georg Pfotzer conducted several balloon experiments to measure ionizing secondary particles at altitudes over 20 km [17]. Their findings revealed what has become the well-known Regener-Pfotzer maximum which is a peak in the radiation flux in the atmosphere. Typically, the peak lies in the 15 km to 20 km range, but the exact altitude of the Regener-Pfotzer maximum is dependent on several factors such as time of year, solar activity, and

geomagnetic latitude [18]. Little variation is experienced in lower latitudes due to the geomagnetic rigidity exceeding 10 GV, but it has a higher effect in higher latitudes. This maximum can be seen in absorbed dose measurements and can serve as a benchmark for sensors. Interestingly, NASA's RaD-X experiment found that the biological dose equivalent does not peak with the Regener-Pfotzer maximum but rather continues to increase with altitude [19].

The most abundant of the secondary particles are protons, neutrons, and pions [20]. The pion decay process subsequently results in the electromagnetic cascade component of the shower, and the interactions of the protons and neutrons subsequently form the nucleon cascade component of the shower. The separation of the shower into these two components allows for a variety of detection techniques. Radio measurements [1] [21], water-Cherenkov detectors [22] [23], and particle scintillators [24] and are often used for measuring the two cascades and can be used simultaneously in various configurations to get a detailed snapshot of an air shower. Detecting multiple types of particles or "messengers" to study different phenomena in the universe is known as multi-messenger astronomy, and it is becoming increasingly important in the study of the sources of cosmic rays as new measurement methodology is developed. Radiation dose contributors for low- to mid-altitude ranges are shown in Figure 1.2.1.

1.3 Monitoring Radiation

The International Commission on Radiological Protection (ICRP) classifies commercial airline crews and astronauts as radiation workers [25]. Monitoring the radiation exposure for individuals such as commercial airline crew members or astronauts is critical for maintaining personal health. Increased exposure to radiation increases an individual's risk of developing cancer. Additionally, it has been found that female airline crew members experience higher rates of miscarriage. A study performed by Grajewski et al. showed that there is a 70% increase in the risk of a miscarriage for flight attendants that received a dose of 0.1 mGy or more during their first-trimester [26].

A study performed from 2003 through 2006 by the United States National Council on Radiation

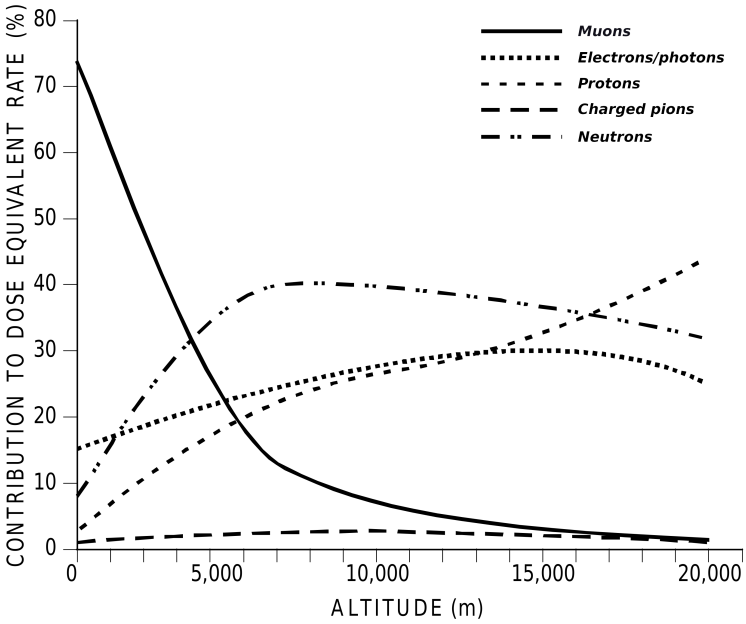

Figure 1.2.1: A breakdown of contribution to dose from secondary particles as a function of altitude. Commercial airline flights are typically in the 10 km to 13 km range; note the high presence of neutrons. This plot is sourced from Ref. [3].

Protection and Measurements (NCRP) reported that the largest average effective dose was in airline crews at about 3 mSv annually [27]. Despite this, the radiation exposure of airline passengers and crews is not actively monitored and relies heavily on computational prediction models, as described by Mertens [20]. He also gives a detailed description of the dose received on various types of flights, including those which are airborne during solar storms, as well as limits set by different government bodies. For example, a single solar storm event while on a high-latitude flight or 5 to 10 trips at high-latitude flight routes (in the absence of solar storms) can exceed the ICRP 1 mSv effective dose limit for public or prenatal planned exposure situations [20].

With regard to astronauts, NASA established a standard in 2007 for limiting an astronaut's exposure to ionizing radiation over the individual's career. The limit per individual is set to "not exceed 3 percent risk of exposure-induced death (REID) for cancer mortality at a 95 percent confidence level" [28]. While these guidelines are certainly pertinent for astronauts aboard the ISS, it is particularly critical for longer duration missions such as those concerning the Moon or Mars.

Due to the lack of atmosphere and magnetosphere, the surfaces of both the Moon and Mars receive higher doses of radiation compared to the surface of the Earth. On the Moon, the annual exposure caused only by GCRs is about 380 mSv during solar minimum and about 110 mSv during solar maximum, but the GCR contribution to annual dose on the Earth's surface is about 2.4 mSv [29]. Measurements over the course of 300 martian sols (1 martian sol is about 24 hours and 39 minutes) made by the Curiosity Rover shows that the GCR dose rate varied from 180 µGy to 225 µGy per day during the maximum of Solar Cycle 24 [30]. The time spent in space must also be taken into consideration when discussing trips to Mars. By using measurements from Curiosity, it is estimated that a round trip to Mars that consists of a 180 day (both ways) transit between planets and a 500-day surface mission will result in a total dose equivalent of about 1.01 Sv [30]. Of course, this amount will vary depending on the shielding provided by the space vehicle and the activity of the Sun.

Mertens states that the atmospheric radiation environment is space-dependent as well as time-dependent, with emphasis on interplanetary and magnetospheric processes. NASA's Nowcast of Atmospheric Ionizing Radiation for Aviation Safety (NAIRAS), what Mertens describes as a "significant step forward in quantifying and documenting aircraft radiation exposure," is a real-time computational model designed to model atmospheric radiation specifically for airline passengers and crews. While this model has advantages over other models, it remains far from perfect. NAIRAS *underestimates* the radiation that is experimentally measured in the atmosphere at mid to low latitudes, with some differences at over 50 percent. Figure 1 from Ref. [31] shows a comparison of models of dose rate as a function of atmospheric depth produced by the NAIRAS, CARI-7, and PHITS computational software. This comparison reveals a deviation between NARIAS and the other two models towards the top of the atmosphere as well as at the surface of the Earth. In fact, data from the CRaTER project highlights this discrepancy between observed and predicted dose rates. Schwadron, Blake, et al. state that the analysis of the data from the CRaTER project has revealed that the observed dose rate exceeded the prediction models by about 10 percent [32]. This discrepancy between observation and prediction highlights an important issue with our current

methods of monitoring radiation which propagates beyond the realm of scientific experiments. The aforementioned behavior from the sun remains extremely difficult if not impossible to accurately model with computational methods. This behavior can be combated with the use of experimental data as demonstrated by NAIRAS, thus reducing the dependency on computational models.

1.4 Active Monitoring of the High Altitude Radiation Environment

Actively monitoring the dose of airline crews can be easily accomplished by equipping each individual with a radiation monitoring badge. These badges simply report an accumulated dose over a period of time, so to monitor the detailed radiation environment in which these people occupy, a more sophisticated system is necessary.

While not the main intent of this experiment, this work supports the development of a compact and portable dosimeter which can be used in a wide range of applications, such as airline flights. This dosimeter provides a more detailed analysis of the environment that the user was in by measuring dose amounts, linear energy transfer (LET) spectra, and a list of the particle types based on their morphology. Various detectors capable of making such measurements already exist, but many of them are either large in size or expensive. Examples include the tissue equivalent proportional counter (TEPC) by FarWest Technologies and the RaySure detector by QinetiQ. Both of these devices are excellent in performance but are not portable or cost-effective for the purpose of personal dosimetry. A more compact dosimeter example would be the total ionizing dose (TID) detector from Teledyne Microelectronic Technologies; however, this device only measures the ambient dose and is not able to report individual particles or LET.

Recent interests have developed around the use of pixel detectors as dosimeters. The central focus of this thesis is to examine this application of pixel detectors and how they fit the criteria as compact, low-cost dosimeters that produce high-quality measurements.

Chapter 2

The MiniPIX Pixel Detector

Pixel detectors are an attractive asset for modern experimental physics, especially in space applications that have strict space and weight limits. This is emphasized by the fact that Medipix-based pixel detectors have been in use on the International Space Station (ISS) since 2012 [33]. The reason is that pixels detectors are generally very small and compact, and this property is highlighted by the MiniPIX, a specific device which uses a Medipix chip, and has the dimensions and weight comparable to that of a typical USB flash drive.

2.1 Semiconductor-Based Pixel Detectors

Semiconductors have seen wide-spread use in all areas of electronics development, and pixel detectors are certainly no exception.

Diodes are made up of a p-n junction. To form this junction, a p-type semiconductor is joined to an n-type semiconductor. A p-type or n-type material is created by doping the material with the proper charge carriers; doping with negative charge carriers, typically electrons, results in an n-type material, and doping with positive charge carriers, typically holes, results in a p-type material. Separately, the two types are charge neutral, but charges can flow across the junction when the two materials are joined together. The process of charges flowing from one type to the other is called diffusion, and the region where this takes place is called the depletion region and contains almost

no charge carriers. In the depletion region, the positive and negative charges recombine, and the spatial charge distribution between the p-type and n-type material results in an electric field across the junction which points from the n-type to the p-type material. This potential sweeps any charge carriers subsequently created in this region to either side of the junction. Negative charges move toward the n-type material, and positive charges move toward the p-type material. An electric field, a bias, can be applied across the joined structure to widen the depletion region.

Jakubek [34] explains the general structure used by most semiconductor pixel detectors and how p-n junctions pertain to radiation detection, but it is outlined as follows. A pixel detector consists of a semiconductor sensor, which is the region in which the charge deposition occurs, and read-out electronics, which perform the signal processing. The bias applied across the junction in a semiconductor sensor is usually large enough to result in a depletion region which is as wide or wider than the thickness of the detector. By doing this, the detector will be completely depleted of excess charge carriers and results in a detector with a volume that is entirely sensitive to radiation and a faster charge collection time [4]. When an ionizing particle, i.e., radiation, creates charges in the depletion region of the sensor, the charges are swept to the anodes and collected and processed by the read-out electronics. Each pixel contains its own set of read-out electronics which consists of an amplifier, threshold discriminator, and counter, essentially making each pixel a "mini-detector."

There are two possible constructions for pixel detectors: monolithic and hybrid With the monolithic construction, the device is made up of one chip with the read-out electronics on the surface of the chip, and the bulk is used as the sensor. The limitation is that monolithic devices can only be constructed from silicon. With the hybrid construction, the device is made of two chips. One chip is the read-out electronics and the other chip is the sensor, both of which are joined together after fabrication. This does not limit the sensor to silicon, and other materials such as GaAs or CdTe can be used. There are different families of pixel detectors, but only one family of chips is relevant to this thesis: the Medipix family.

2.2 The Medipix and Timepix Chips

The Medipix read-out chips are a family of chips developed over technological generations by the Medipix Collaboration at CERN [35].These chips were originally designed for applications within high energy physics, but it was soon realized that they were incredibly robust. One of the goals of the Medipix2 Collaboration was to make this technology easily accessible to other fields [36]. Popular areas of use include dosimetric measurements [37], neutron imaging [38], medical physics [34] [39], and x-ray imaging [40]. The Medipix2 chip is composed of a 256 by 256 array of pixels, each 55 µm by 55 µm in size and 300 µm in thickness. The Timepix chip is a modified version of the Medipix2 chip [36] which adds additional functionality that allows it to be used in dosimetry applications. A more technical description of the Medipix2 and Timepix chip layouts can be found in Ref. [34] and Ref. [36].

2.2.1 Timepix Signal Processing

The advantage of the Timepix chip over the Medipix2 chip is that each pixel is able to operate independently of one another in one of three modes. The modes are Medipix (counting), time of arrival (TOA), and time over threshold (TOT). Medipix mode will count the number of times the pixel's signal rises above the threshold. In TOA mode, the pixel will count the length of time from when the signal of the pixel is above the threshold until the end of the frame. A pixel in TOT mode will count the length of time that the signal of the pixel is above the threshold which allows for precise energy and track measurements.

The measurement process begins with a particle interacting with the sensor. The interacting particle generates charge carriers within the depletion region which are then swept to the anodes as input for the read-out electronics. The input is sent to the preamplifier which amplifies the signal and results in a sharp peak. This amplified signal is then sent to the discriminator which compares the signal to the threshold values. The discriminator will respond according to which mode the pixel is in. In Medipix mode, the counter increments by one each time a peak is above the

threshold. While in TOA mode, a signal above the threshold causes the discriminator and counter to remain active until the end of the measurement. When in TOT mode, the discriminator is active only while the signal is above the threshold, and the counter will increment with the clock until the signal falls below the threshold. This time interval in which the signal is above the threshold is proportional to the deposited energy. The pixel calibration and energy calculation is discussed further in Section 2.4.1.

2.3 MiniPIX Device Characteristics

The particular detector that will be examined is the MiniPIX which is a silicon-based hybrid pixel detector and can be purchased from ADVACAM [41] with a silicon thickness of 300 µm or 500 µm. The MiniPIX device is one such pixel detector that uses the Timepix chip.As such, it is capable of detecting individual particles such as electrons or photons and returning information such as the energy the particles deposited into the detector. By analyzing data recorded by the MiniPIX, one can make important measurements regarding the LET spectra and absorbed radiation. Figure 2.3.1 shows the MiniPIX plugged into a computer.

Figure 2.3.1: Image of the MiniPIX plugged into the USB port of a computer.

The MiniPIX demands very little in terms of electrical requirements. The power and data interface is packaged into a USB 2.0 port, so the device can be plugged into and operated by any modern computer. It needs a 5 V supply voltage and will draw a maximum of 500 mA when the chip is active, equating to a maximum of 2.5 W power dissipation. Typical operation will lie well below this maximum.

The recommended operating temperature of the MiniPIX is 0 °C to 70 °C. In a lab environment, an active device with no attached heat sinks will typically sit in the 40 °C to 50 °C range. Outside of a lab environment, thermal management becomes important, and, in warmer settings, heat sinks become a necessity. The sensor becomes noisy when the temperature of the device gets too high. Pixels are falsely activated, resulting in a quick decline in the quality of the data. An example of this is shown in Figure 2.3.2a. If the temperature becomes too high, the sensor is flooded and almost every pixel is activated resulting in useless data, as shown in Figure 2.3.2b. Ref. [42] highlights the temperature dependence of a pixel's energy threshold and presents a method for an in-situ calculation of a new device calibration at any temperature.

The MiniPIX is shipped with the PixetPro software. PixetPro is an application with a graphical user interface that allows the user to easily interface with a Medipix detector as well as the Pixet API which allows the user to use the Python programming language to control and operate the device. The Pixet API allows fine control of the device and allows the user to fully automate the operation of the device without the use of PixetPro. It also allows the user to monitor the temperature of the device with its built-in temperature function. PixetPro and the Pixet API are compatible with many Medipix devices, not just the MiniPIX.

Another attractive quality of the MiniPIX is its price. The device along with its associated software costs about a few thousand dollars which is rather inexpensive for a radiation detector. Considering the performance of the MiniPIX, the quality of data it acquires, and the potential applications of the device, the cost is even further minimized. The USB interface and compact package open applications for use as a programmable and portable dosimeter. The device can

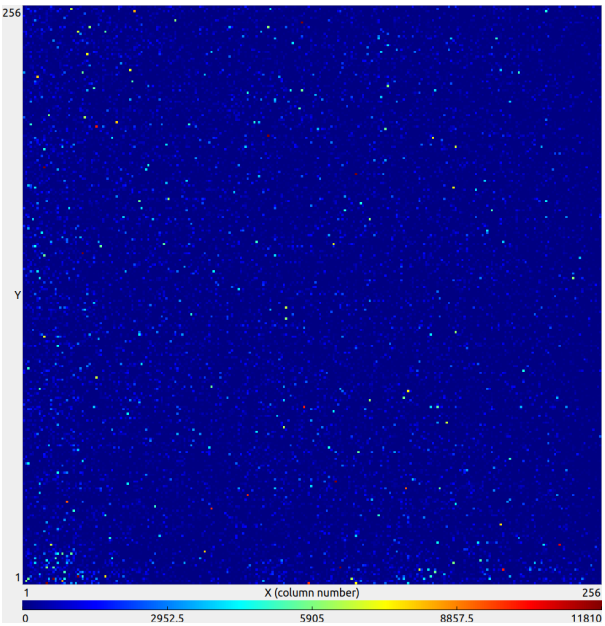

(a) An example of a frame recorded while the device temperature exceeded the recommended maximum operating temperature.

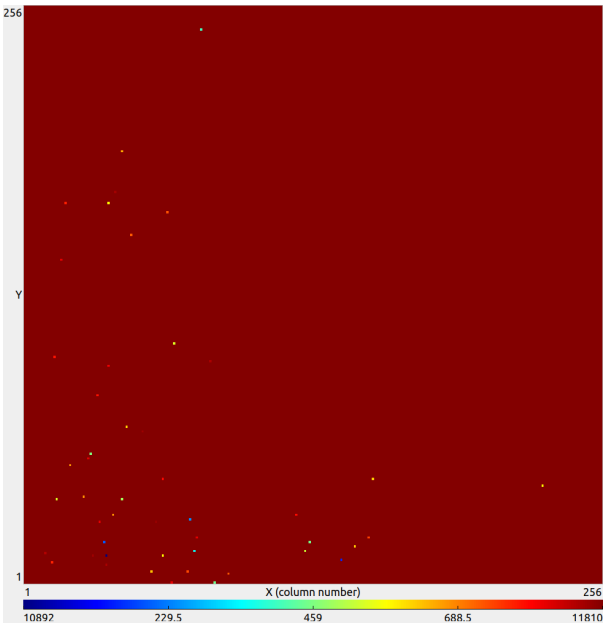

(b) An example of a flooded frame recorded when the device temperature greatly exceeded the maximum operating temperature (the red pixels are pixels which returned their maximum possible value).

Figure 2.3.2: Examples of the temperature dependence of Timepix pixels. Both data frames feature incorrect data. Note the energy scale below the images.

operate independently, allowing remote calibration and data transfer and providing real-time feedback about its local radiation environment. When used in conjunction with hobby electronics, as discussed later in the thesis, the process of building such a tool becomes relatively user-friendly and cost-effective. It is important to keep in mind that the cost of such tools will only decrease as technology continues to develop, and dosimeters such as this will become much more widely accessible to individuals and companies alike.

2.4 Operational Parameters

The device operates similarly to that of an optical camera in that the device has a digital shutter and an associated, user-defined shutter time. At the beginning of each measurement, the energy value of each pixel is zero, and the value of a pixel will change once the pixel measures energy above the user-defined threshold. After the specified shutter time, the readout electronics will

collect the recorded ADC counts from each pixel and output the data to the USB interface, and the cycle repeats. The shutter time is a particularly important parameter that must be chosen carefully depending on the environment and desired measurements, especially if data storage space is a concern. If the shutter time is too short, the device will record an abundance of empty or mostly-empty data frames that will rapidly consume the computer's storage space. However, if the shutter time is too long, the data may become difficult to analyze if particle clusters begin intersecting one another. Techniques can be used to automatically adjust the shutter time of the device depending on the intensity of the radiation, as shown in Ref. [43], which was in use aboard the ISS due to the wide-range of radiation exposure experienced on the station. An example of this undesired intersection can be seen in Figure 2.4.1. The example shown is a rather simple instance of intersecting tracks since the particles are relatively low energy. Such an event could be resolved using more sophisticated analysis software to identify the two separate tracks and approximate the track energies at the intersection, but approximations for intersections of higher energy tracks (or an intersection between a high energy track and a low energy track) may not be as accurate considering the wider range of possible values the pixels can have.

Another important device parameter is the energy threshold. Each pixel has a preamplifier that can be programmed with an energy threshold independent from the other pixels. Similar to the shutter time, care must be taken when choosing an energy threshold for the sensor so that the pixels do not detect erroneous background noise and can detect particles in the desired energy range. Generally, the threshold will be chosen such that low energy background radiation will not be recorded by the device. For this work, the device operated in TOT mode and was calibrated according to the process outlined in the following section.

2.4.1 Calibration

The response of each pixel is unique, so each pixel needs to be calibrated. The TOT calibration procedure used in this experiment is one proposed by Jakubek [44] and was carried out by Dr. Stuart George at the UH campus using ^{55}Fe, ^{241}Am, and Sn fluorescence. The procedure yields

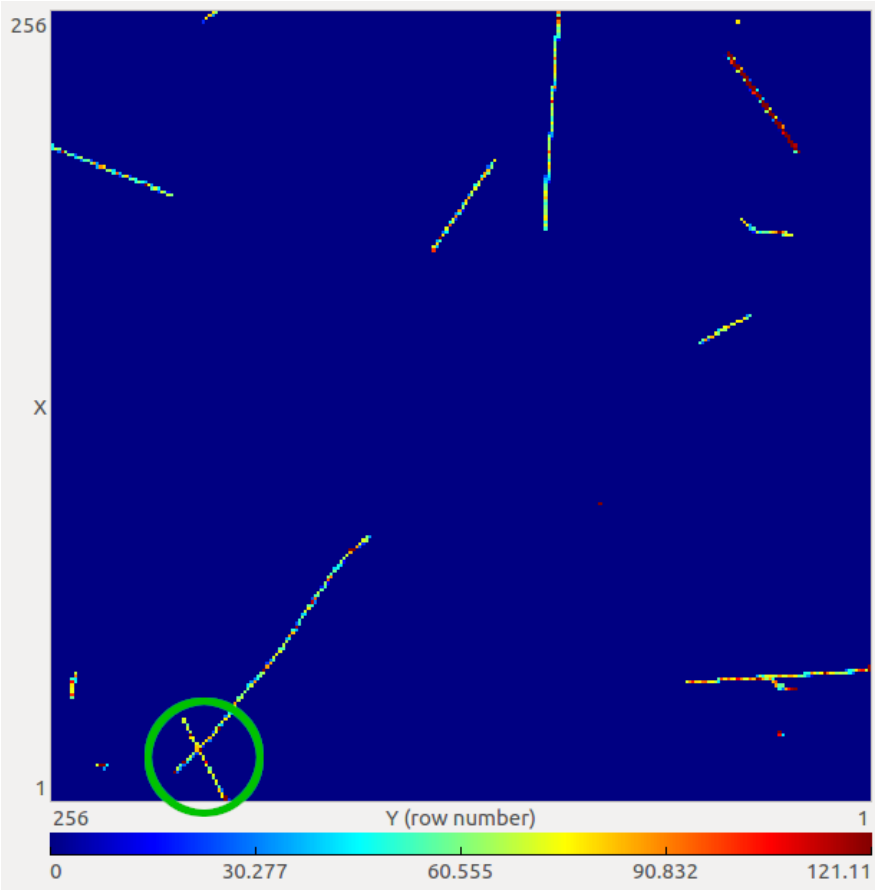

Figure 2.4.1: An example of two intersecting tracks near the bottom left corner of the frame marked by the green circle.

four calibration parameters, a, b, c, and t, for each pixel which relates the TOT response to the energy by

$$TOT(E) = a + bE - \frac{c}{E - t}. \tag{2.4.1}$$

The resulting values of the parameters are saved to text files which are read by the MiniPIX upon initialization.

2.5 Medipix Output

Data frames from the MiniPIX is saved in a human-readable, array-like format. Since a single pixel in the sensor array has a single numerical energy value associated with it, the output file can be used to directly reconstruct the 256 by 256 pixel layout of the sensor. Alongside the data frame, metadata is saved containing information such as the frame number, chip-type, start time, Timepix mode, shutter time, energy threshold, and various other device parameters. If desired, the recorded output can be loaded by PixetPro and viewed using its GUI, producing an image similar to that shown in 2.4.1.

2.5.1 Particle Morphology

There are various methods to processing and classifying incident particles upon a Timepix sensor. Perhaps the most common method is based on track morphology in which a clustering algorithm is used to group together non-zero energy pixels [4] [45]. Being an active field of research, more recent approaches have taken further steps in attempt to extract more detailed information from the pixel data. One approach seeks to determine the azimuth and zenith angles of incident particles by analyzing the energy dispersion across the pixels [46]. Some have devised fast machine learning techniques to classify particles by species [47]. Other techniques are using two or more Timepix devices in parallel to either broaden the angular resolution [48], to increase neutron detection [49], or to construct a telescope with multiple layers of sensors to achieve high track pointing precision [50].

In this thesis, classification was done using a particle's morphology. There are six classes of shapes, each indicating different possible types of particles. Figure 2.5.1 shows the different classes and the possible particle which created the track. It is important to note that the morphology does not give the exact identity of the incident particle, but good inferences can be made in conjunction with the energy of the particle.

The morphological nature of the data allows for the calculation of several dosimetric quantities. The absorbed dose in silicon can be converted to the equivalent dose in biological materials such as

Type	Inner Pixels	Length/ Width Ratio	Other Criteria	Example Tracks
Small Blob	0	-	1 or 2 Pixels, 3 if L shape, 4 is square	
Heavy Track	> 4	> 1.25	Not S.Blob Density > 0.3	
Heavy Blob	> 4	< 1.25	Not H.Track Density > 0.5	
Medium Blob	> 1	< 1.25	Not H.Blob Density > 0.5	
Straight Track	0	> 8	Not M.Blob Minor axis < 3 pixels	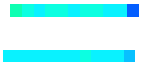
Light Track	-	-	Not S.Track	

Figure 2.5.1: A table showing the different morphological classes, their criteria, and an example of a cluster as recorded by the pixel sensor. This graphic is sourced from Ref. [4].

cells, organs, or tissues. Performing such a conversion requires the use of a quality factor, Q. The quality factor was first defined by the ICRP in publication 6 in 1964, but the relevant definition in this application was defined in ICRP publication 60 in 1990 [25]. Since then, the concept of radiation weighting factors was introduced as a successor to quality factors, but the quality factor calculation remains suggested for radiation monitoring applications [51]. In ICRP 60, Q is defined as a function of LET as shown in Equation 2.5.1, but various definitions of Q have defined it in terms of other track properties (e.g., Ref. [52] defines it in terms of particle charge and energy).

$$Q_{60}(LET) = \begin{cases} 1 & LET < 10\,\mathrm{keV\,\mu m^{-1}} \\ 0.32LET - 2.2 & 10 \leq x \leq 100 \\ \dfrac{300}{\sqrt{LET}} & LET > 100\,\mathrm{keV\,\mu m^{-1}} \end{cases} \tag{2.5.1}$$

The plot of this function is shown in Figure 2.5.2. This quality factor is related to dose equivalent,

H, by

$$H = DQ_{60}. \tag{2.5.2}$$

Absorbed dose has units of Gray Gy and dose equivalent has units of Sievert (Sv). The Gray is simply the energy deposited by ionizing radiation, but the biological damage due to radiation is different depending on the type of radiation that deposited the energy. The Sievert takes into account this difference by including weighting factors.

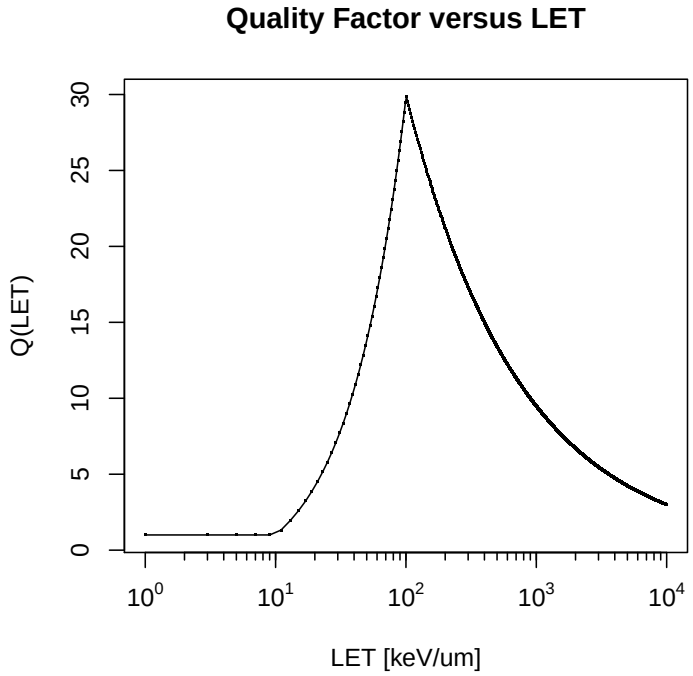

Figure 2.5.2: Q_{60} as defined in ICRP Publication 60.

Some popular methods of calculating Q factors between materials make use of Monte Carlo simulations [53] [54]; however, since LET can be calculated for each particle recorded in the Medipix data, the H can be calculated per particle [4] [55] [56] with the use of the Q_{60} function.

The characteristics of measured particles noticeably change depending on the ambient radiation field. A detector closer to the Earth's surface will more frequently measure small blobs or light

tracks, but a detector at higher altitudes (i.e., aviation altitudes or beyond) will more frequently see heavy tracks, heavy blobs, and straight tracks. In the following chapter, the resulting dose and the LET measurements made by a MiniPIX traversing vertically through the atmosphere will be examined.

Chapter 3

Atmospheric Dosimetry with a MiniPIX Device

Determining dose rates as a function of altitude has been of interest for many decades, but due to the recent radiation flux increases observed in the atmosphere, an active approach needs to be taken. The experimental aspect of this thesis focuses on the application of a MiniPIX device as a dosimeter, and this work aims to contribute to a foundation of using Medipix-based devices for dosimetric applications. A mock-up ISS module was constructed in order to emulate the environment that astronauts aboard the actual ISS live in. The purpose of this is not to make measurements to directly compare to the actual ISS but to observe how a modeled environment responds to the changing radiation profile in the atmosphere. The data from the MiniPIX inside the mock-up structure was analyzed to determine absorbed dose rates, particle types, and the number of each type of particle found at various altitudes between a range of 0 km to 35 km above the surface of the Earth.Chapter 4 explores the use of simulations to validate the results obtained from atmospheric dosimetry studies, including those obtained by the MiniPIX in this study.

3.1 A Typical HASP Mission

The High Altitude Student Platform (HASP) [57] is a balloon program hosted by NASA and the Louisiana Space Consortium that sends scientific payloads to the stratosphere on a high altitude balloon. HASP missions operate on yearly cycles. Each cycle begins roughly in the October of the year prior to the launch (e.g., the 2019 mission began in October 2018) with the release of the program application. Student-led teams apply to the program and, if accepted, design and build a scientific payload that will be launched into the stratosphere on a high altitude balloon. The intent of the program is to provide university students the opportunity to gain experience in real-world research applications which will help build relevant skills and foster interest. After being accepted, student teams from universities around the world spend the next couple of months creating a design plan for their payload. Included in the application are mission objectives, mechanical drawings, electrical diagrams, and operation procedures. Accepted teams are announced in January, and the teams spend the next seven months constructing the payload. A week in July is spent at a NASA base integrating each student payload into the HASP balloon systems to ensure proper data communication and power distribution. Following the integration, the teams have about a month and a half until the balloon is launched from Fort Sumner. It takes a few hours for the balloon to reach the float altitude of about 30 km to 35 km where the balloon will spend the remainder of the flight. Typical float times are about 8 hours. Upon termination, the payloads are powered down, and the balloon plummets to the Earth with a parachute, and the payload gondola is retrieved about a couple days later. Student teams then spend the next few months analyzing the flight data. The cycle ends with the submission of a final report in December detailing the performance and data results of the payload.

The mock-up ISS structure was housed in the 2019 HASP mission as a subsystem aboard the University of Houston (UH) payload. The overall objective of the UH payload was to monitor the radiation environment as the balloon increased in altitude, observe the performance of organic solar cells in a near-space environment, and collect stratospheric microorganisms. The HASP 2019

balloon launched from Fort Sumner, New Mexico on September 5th, 2019 at 13:03:15 UTC and terminated later that day at 23:17:56 UTC.

3.2 Development of a Real-Time Dosimeter

As part of the 2018 UH HASP mission, a software tool was developed which allowed for real-time analysis of MiniPIX data during the balloon flight. The analysis produces the particle counts and radiation dose, which can be downlinked from the balloon to Earth and viewed in real-time. Credit for the development of this real-time dosimeter is given to Andrew Walker, a former UH student, which can be found on Github at `https://github.com/andrewi66doe/MiniPIX-RPI-Dosimeter`. This real-time dosimeter was adapted to the 2019 mission. The 2019 payload contained two Medipix devices, so the dosimeter was expanded to accommodate two sensors and produce separate data for each sensor. The dosimeter is a robust and readily expandable platform that provides an excellent foundation for using Medipix devices in atmospheric applications or, more generally, less-permanent applications. The MiniPIX was calibrated by Dr. Stuart George at the UH campus using the procedure outlined in Section 2.4.1. The sensor used in this experiment has a thickness of 300 µm.

3.2.1 Hardware

The dosimeter uses a Raspberry Pi 3 Model B as the computer. The Model B's 1 GB RAM and 1.2 GHz processor provides enough computational power to simultaneously support one or more Medipix devices, but newer Raspberry Pi models would certainly offer increased performance to support a larger array of devices. The main advantage of using a Raspberry Pi is that Medipix devices can be directly plugged into its USB ports, and the overall package remains portable as well as space, weight, and power-efficient. With one active MiniPIX, the dosimeter draws about 1 A of current. Another advantage of the Raspberry Pi is the use of microSD cards for data storage. These cards have very high storage density with newer cards possessing 1 TB of space, and they

can easily be swapped in to and out of the dosimeter. MISS used a 64 GB microSD card which was more than enough for a balloon flight of this duration.

3.2.2 Analysis Procedure

An analysis technique similar to the one described by George [4] was used by the dosimeter to analyze the Medipix data in real-time. The following is a description of this analysis technique. The first quantity of interest is the absorbed dose by the silicon sensor, D_{Si} due to a cluster which is defined as follows

$$D_{Si} = \frac{E}{M_d}. \tag{3.2.1}$$

Here, E is the total energy of the cluster, and M_d is the total mass of the detector. The use of this relation requires the assumption that the incoming particle penetrates the entire thickness of the sensor and does not stop within the sensor. Since the mass of the sensor is constant, it is a rather straightforward calculation for the dose. E is obtained by using a typical flood-fill clustering algorithm on a Medipix frame to group all touching pixels with non-zero energy and summing their energy values together. One cluster corresponds to a single particle count.

The second quantity of interest is the LET. The formal definition of LET, given by ICRP 60 [25], is

$$LET = \frac{dE}{dl}; \tag{3.2.2}$$

however, a simplified form can be applied to the silicon Medipix sensor as given by Ref. [55]. LET in the silicon sensor is calculated as follows

$$LET_{Si} = \frac{E}{L}, \tag{3.2.3}$$

where E is the same energy used for the D_{Si} calculation, and L is the three dimensional length of the particle track in the sensor. To calculate L, a minimum-area bounding box is constructed around the particle track with a linear least square fit line which intersects the bounding box. A

visual example of a bounding box can be seen in Figure 3.2.1.

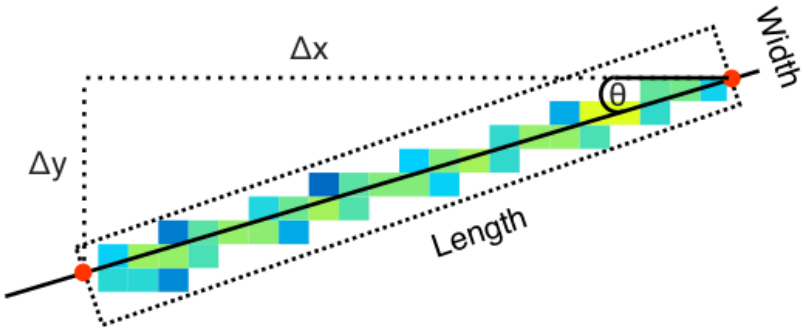

Figure 3.2.1: An example from of a bounding box around a particle track (the dotted black box surrounding the particle track), and the fit line (the solid black line along the particle track). This visual is borrowed from Ref. [4].

The points of intersection can be used to calculate the length of the fit line which is the projected track length, L_p. Using L_p and T, the thickness of the sensor, the following relation can be used to calculate L,

$$L = \sqrt{L_p^2 + T^2}. \tag{3.2.4}$$

With T being a known property of the sensor, LET_{Si} can be calculated on a per particle basis.

3.3 Mock-up International Space Station - MISS

With the strong software foundation that resulted from the first two UH HASP missions, it was natural to use this foundation towards the development of a more practical application. Considering the relevance of active radiation monitoring, the idea to develop a model ISS, what will be referred to as the Mock-up International Space Station (MISS) from here on, was executed as a sub-experiment aboard the 2019 HASP mission. The goal of MISS was to model and observe the change in the radiation field introduced by the structure of the environment. The placement of MISS on the UH HASP payload is shown in Figure 3.3.1.

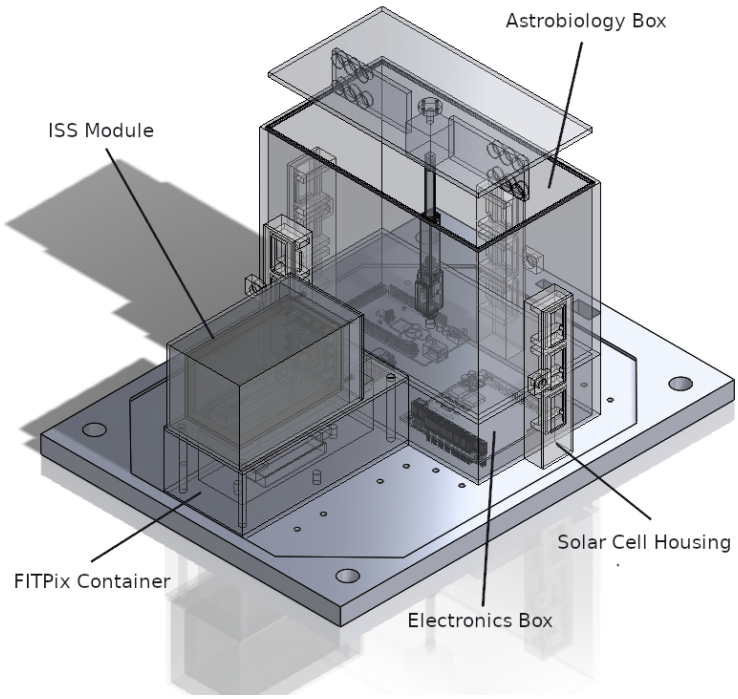

Figure 3.3.1: Layout of the 2019 UH HASP payload showing the location of MISS. The only obstruction between the MiniPIX and the atmosphere is the MISS structure.

3.3.1 Construction and Materials

The shielding used for an ISS module differs depending on which space agency constructed the module. Figure 3.3.2 shows the structures used by NASA, JAXA, and ESA.

Typical aluminum alloys are 6061-T6 for the bumper (i.e. outer wall, the wall exposed to space) and 2219-T87 or 2219-T851 for the rear wall (i.e. inner wall, the wall containing the atmosphere). Kevlar 29 style 710 and Kevlar KM2 style 705 fabrics are usually used for the Kevlar layers. The multi-layer insulation (MLI) is a thermal blanket for mitigating energy transfer and not for shielding debris. The overall structure is capable of shielding against 1.3 cm diameter aluminum spheres traveling at 7 km/s normal to the surface, and each layer of the shielding serves a different purpose in an impact event. A micro-meteoroid or orbital debris (MMOD) particle incident on the bumper is broken into smaller pieces which are laterally dispersed. The broken pieces impact

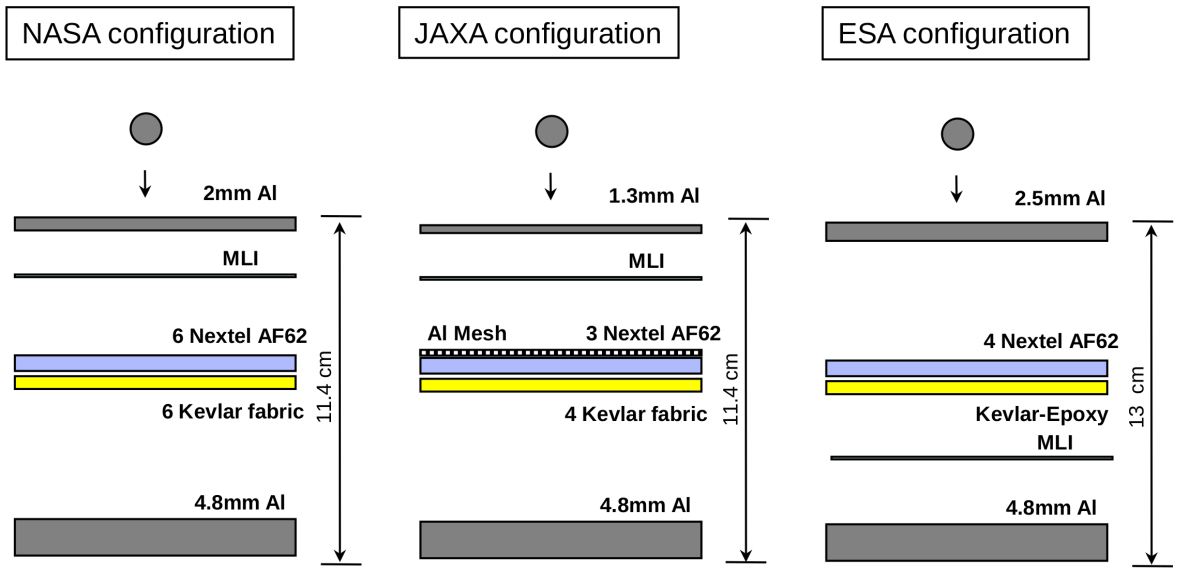

Figure 3.3.2: ISS shielding used by different space agencies as given by Ref. [5]. The number preceding the words "Kevlar" or "Nextel" refer to the number of fabric layers.

the Kevlar and Nextel layers which slow the debris cloud's expansion. The rear wall then stops any remaining debris particulates. The construction of MISS was modeled after NASA's shielding configuration.

The structure of MISS is a rectangular prism consisting of various layers that match the thicknesses of the NASA shielding configuration. MISS was designed from the inside-out meaning the inner-cavity containing the MiniPIX was given a specified volume, and the material layers were given dimensions such that each layer was tightly wrapped around one another with little to no gap between layers. Wrapping 6 layers of each fabric over itself results in the dimensions shown in Figure 3.3.3. To construct the metal layers, plates for each side were cut then welded to each other. The only face not welded to the structure was the front face so that the MiniPIX could easily be inserted and removed. The front face was a separate piece consisting of the proper material layers as well as a USB interface to communicate with the inside of the structure. The front plate was attached to the structure with standard screws. The overall dimensions of MISS consist of a 142 mm depth and a 84 mm by 84 mm face. The 3D rendering of the model is shown in Figure

3.3.4. More detailed depictions of MISS' front plate can be found in Appendix A.

To model the ISS as accurately as possible, MISS was designed such that the inner aluminum structure would be pressurized with 1 atm of air. A few days prior to launch, Torr Seal TS10 vacuum epoxy was used to seal any gaps that remained after the module was fully constructed so that the internal pressure would remain constant as MISS climbed through the atmosphere. A sensor was placed inside of MISS to monitor the pressure and temperature.

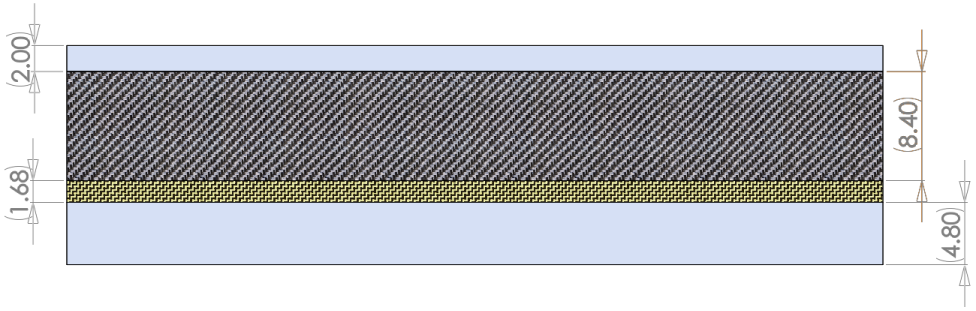

Figure 3.3.3: Cross section of the layers used to construct MISS. All dimensions are in millimeters.

3.3.2 Inaccuracies in the MISS Construction

There were several inaccuracies in the MISS structure that deviated from the exactly modeling the material layers of the NASA ISS module construction in Figure 3.3.2.

The pressure and temperature sensor inside of MISS stopped working just before the launch of MISS, so it is unknown if the internal pressure remained at 1 atm for the duration of the flight. Another inaccuracy of MISS is the use of aluminum 2219-T87 for both of the aluminum layers (the accuracy in the thicknesses of the layers was preserved). Aluminum 6061-T6 is an aircraft-grade material and is largely cost-prohibitive as the material can only be purchased as sheets that cost several thousands of dollars. Additionally, the Kevlar used in MISS is Kevlar 49 fabric. Kevlar 49 has a thickness of 0.28 mm as opposed to the 0.61 mm thickness of Kevlar 29 Style 745. The primary differences between these two grades of Kevlar are differences in their mechanical properties such

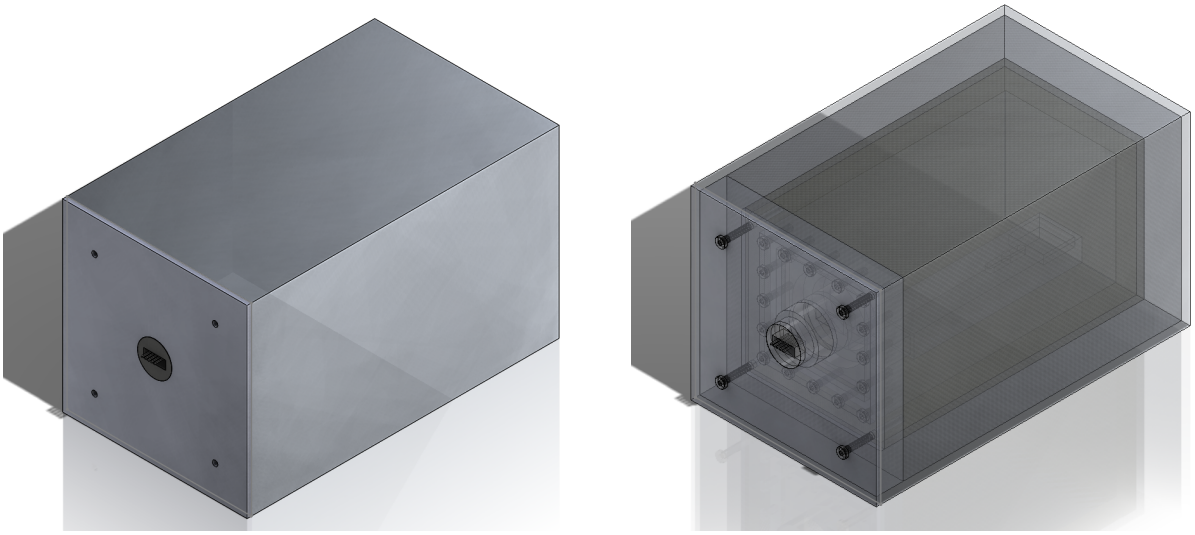

(a) 3D rendering of MISS. (b) 3D rendering of MISS with transparent layers.

Figure 3.3.4: Rendering of the final MISS concept.

as tensile modulus, tensile strength, and others [58]. The effect of this difference in aluminum and Kevlar is thought to be minimal.

Another important difference in the MISS construction is the lack of the standoffs between the layers and the lack of the MLI, but these differences were a necessary sacrifice. Since MISS would be traveling through the atmosphere, air would be present in the gaps between layers whereas a near-vacuum is present in the gaps of the ISS. Incoming radiation could interact with the air particles thus altering the radiation field in a way that is not present on the ISS. Furthermore, each institute's payload was limited to a certain volume aboard the balloon, so it would not have been possible to replicate the necessary gap widths aboard this flight. The lack of MLI shares a similar justification.

Lastly, the Nextel fabric did not arrive prior to MISS' flight. The lead time of the material exceeded the amount of time available before the launch of the project, so MISS lacked the layer of Nextel.

3.3.3 Altitude Calculations

The UH payload featured a pressure sensor to record the ambient atmospheric pressure. This data was used to approximate the altitude of the payload so that the dose could be reported at various altitudes.

The conversion from pressure to altitude is in accordance with the layered atmosphere model established by the U.S. Standard Atmosphere in 1976 [59]. This model features two equations to calculate the pressure P at an altitude h above sea level. The first being

$$P = P_b \left[\frac{T_b}{T_b + \alpha_b (h - h_b)} \right]^{\frac{g_0 M}{R^* \alpha_b}}, \tag{3.3.1}$$

and the second being

$$P = P_b \exp \left[\frac{-g_0 M (h - h_b)}{R^* T_b} \right]. \tag{3.3.2}$$

The first equation corresponds to non-zero standard temperature lapse rate while the second is used when the standard temperature lapse rate is zero. In these equations, the single-valued constants are g_0, M, and R^* which are the Earth's gravitational acceleration at sea level, the molar mass of the Earth's air, and the universal gas constant, respectively. For this work, the values for the constants were taken to be $g_0 = 9.806\,65\,\mathrm{m/s^2}$, $M = 0.028\,964\,4\,\mathrm{kg/mol}$, and $R^* = 8.314\,32\,\mathrm{J/(molK)}$. P_b, T_b, h_b, and α_b are respectively the reference pressure, reference temperature, bottom altitude, and standard temperature lapse rate, all of which are constant for the particular layer of interest.

To solve for the altitude, Equation 3.3.1 and Equation 3.3.2 were rearranged to

$$h = h_b + \frac{T_b}{\alpha_b} \left[\left(\frac{P}{P_b} \right)^{\frac{-1}{\beta}} - 1 \right] \tag{3.3.3}$$

and

$$h = h_b - \frac{R T_b}{g_0 M} \ln \left[\frac{P}{P_b} \right]. \tag{3.3.4}$$

For MISS, only the first four layers are relevant. These layers and their corresponding constants

are defined in Table 3.1.

Altitude [m]	h_b [m]	α_b [K/m]	T_b [K]	P_b [Pa]
0 – 11 000	0	-0.0065	288.15	101 325
11 000 – 20 000	11 000	0.0	216.65	22 632.1
20 000 – 32 000	20 000	0.001	216.65	5474.89
32 000 – 47 000	32 000	0.0028	228.65	868.019

Table 3.1: Definition for the first four atmospheric layers and their respective constants.

3.4 Results from MISS

This section describes the contents of the MiniPIX data, presents its measurements, and compares it to the measurements made during previous UH HASP missions.

3.4.1 Dosimetry Measurements

Over the course of about 5 hours of constant measurement, MISS recorded a total of 15 735 data frames which consumed about 2.1 GB of storage space. This results in a rate of about 0.42 GB/h, highlighting the rapid storage consumption of the Medipix data. Unfortunately, MISS only recorded data during these first 5 hours of the flight. The payload as a whole ceased to function after a mechanical failure in a separate subsystem. This mechanical failure prevented system reboots for reasons that will not be discussed here as they are not in the scope of the experiment, but this malfunction occurred after the balloon had reached float meaning that MISS captured data during the entirety of the balloon's ascent and for a short while at float. As a result, the data captured by MISS reflects the Regener-Pfotzer maximum as well as the relatively constant count and dose profile above the maximum. Based on previous balloon flights, the dose and counts remains constant at float, so the data recorded by MISS would likely have been homogeneous. The most prominent loss due to this failure is likely regarding single particle events which are rare for a short duration balloon flight such as this.

An important feature to note in the data is the gap occurring mid-way between 13:00 and 14:00 UTC. This gap was due to a balloon-wide power shutdown. This shutdown lasted for about 15

minutes, and this period of time when no measurements were taken is noted on the data plots.

Figure 3.4.1a shows the particle counts recorded by MISS during the balloon flight. The number of counts describes the number of particles per frame, and a count measurement was made roughly every 5 seconds. One important feature to note is the Regener-Pfotzer maximum which can be seen at about 12:45 UTC as well as the constant count rate that settles in at 13:30 UTC and continues through to the end of the recorded data.

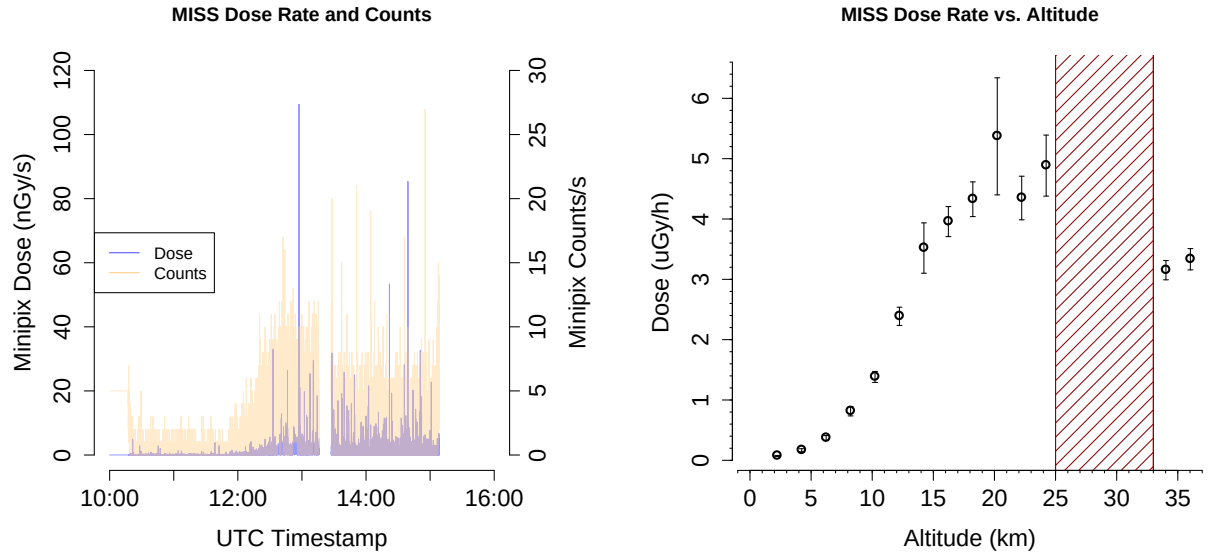

(a) Absorbed dose rate overlaid on the particle counts during flight. Note the gap due to the unpowered balloon just after the 13:00 mark. Each measurement corresponds to one frame.

(b) Absorbed dose binned as a function of altitude from the 2019 UH HASP mission. The striped region marks the range of altitudes during which the balloon was not powered. Error bars are given by the standard error.

Figure 3.4.1: Plots of absorbed dose and particle counts recorded by MISS throughout the balloon flight. The Regener-Pfotzer maximum is clearly visible in the count rate and dose rate.

Figure 3.4.1a also shows the dose measurements recorded by MISS throughout the flight. By summing each dose measurement during the flight, the total dose deposited in the MiniPIX is 7.64 µGy over 4.66 hours resulting in about 1.64 µGy/h averaged over the entire flight. If only considering the relatively constant dose rate at float time (i.e., removing the dose measured during ascent and the Regener-Pfotzer maximum), the total dose is 4.38 µGy over 1.69 hours, which is about 2.59 µGy/h averaged at float. These measurements, as well as those shown in Figure

3.4.1b are in good agreement with other balloon missions such as the BEXUS stratospheric flights [60]. BEXUS flights took place at a latitude of 68°N, so the reported doses for those missions are slightly higher than the MISS measurements, which is to be expected. Similarly, the MISS results are validated by reports from the Intercontinental Space Weather Balloon Network [61] which features dose measurements taken by stratospheric balloon launches around the world and at various latitudes in 2016. The results from MISS fit nicely within their reported measurements once the solar cycle is taken into consideration. Figure 3.4.4 presents the data frame containing the event that deposited the highest dose, showing the footprint of higher energy particles.

Altitude was calculated using the air pressure measurements from the UH payload with the method described in Section 3.3.3. The dose measurements were grouped into bins with a width 2.0 km starting with a bin of 1.2 km to 3.2 km and continuing up to about 38 km. The only exceptions are one bin with the range of 23.2 km to 24.9 km which is shortened due to the balloon losing power, and the bin starting at 36 km which is has no defined end altitude due to the uncertainty in the pressure sensor's measurements. At near-vacuum pressures and temperatures approaching −40 °C, the pressure sensor becomes much less reliable, so all measurements made after 36 km were grouped into one bin to account for the error. It is acceptable to group the last bin this way since NASA reports a maximum altitude of 37.3 km for the balloon used for this mission which gives this bin a similar width as the other exception. The values in each bin were averaged, and the error was calculated using the standard error

$$SE = \frac{\sigma}{\sqrt{n}}, \tag{3.4.1}$$

where σ is the standard deviation of all samples in the bin and n is the number of samples in the bin. Figure 3.4.1b shows the result of the binning.

The analysis from the cluster identification algorithm is provided two representations. One is in the form of a histogram with a bin width of 150. The histogram clearly displays the distribution of each track type and the number of hits from each track type throughout the flight. The shape of

each track type closely corresponds to the data recorded by a Timepix in mixed radiation field at CERN-EU high energy Reference Field (CERF) which replicates the field produced by cosmic rays in the atmosphere at commercial airline altitudes [4]. The other representation is with a density plot that provides a good sense and a clear visual of the frequency of the various cluster types with respect to the cluster energy. The noteworthy feature of the density plot is the fairly close alignment of the light track, straight track, and medium blob peaks along the energy axis. These three cluster types commonly correspond to lighter particles (e.g. electrons, positrons, muons, and protons) within a specific energy range which is a good indication of a properly calibrated sensor.

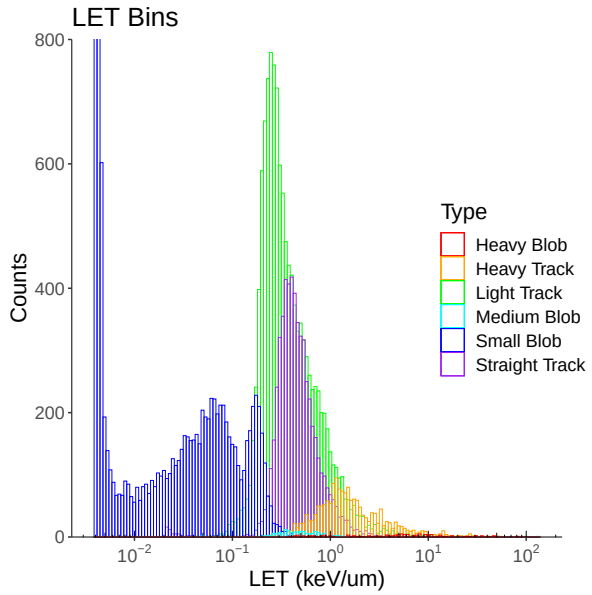

(a) LET histogram with a linear "Counts" scale.

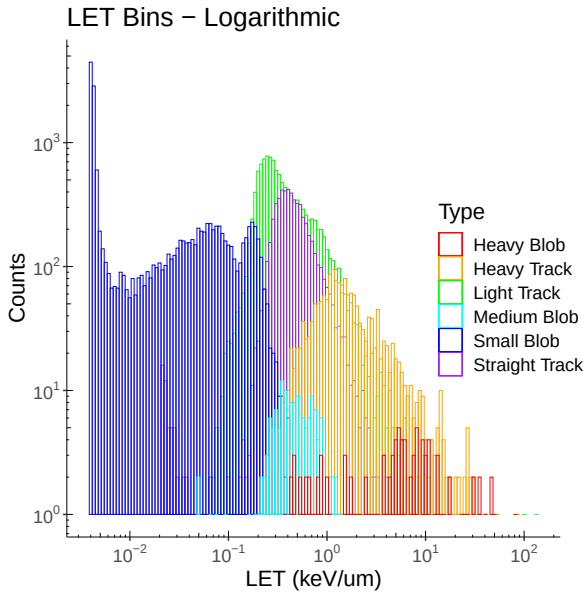

(b) LET histogram with a logarithmic "Counts" scale to highlight the relative counts of the medium blobs and heavy blobs to the other cluster types.

Figure 3.4.2: LET histograms for each particle cluster type. Both figures show the same data but with different scales for the vertical axis.

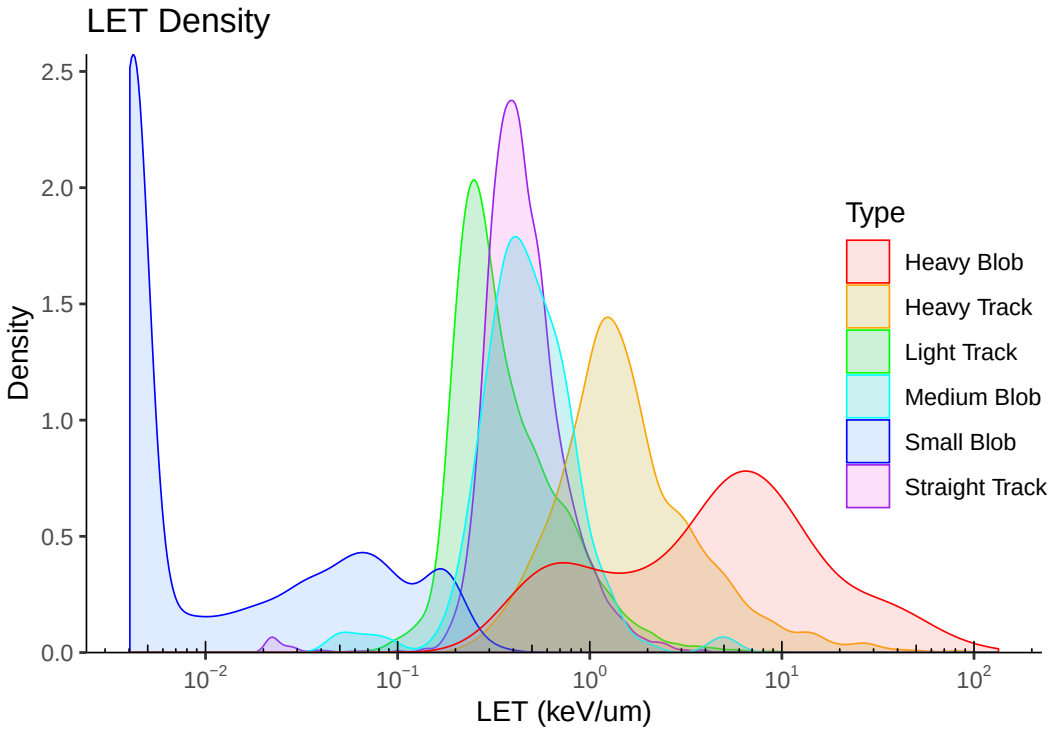

Figure 3.4.3: LET density distribution by cluster type.

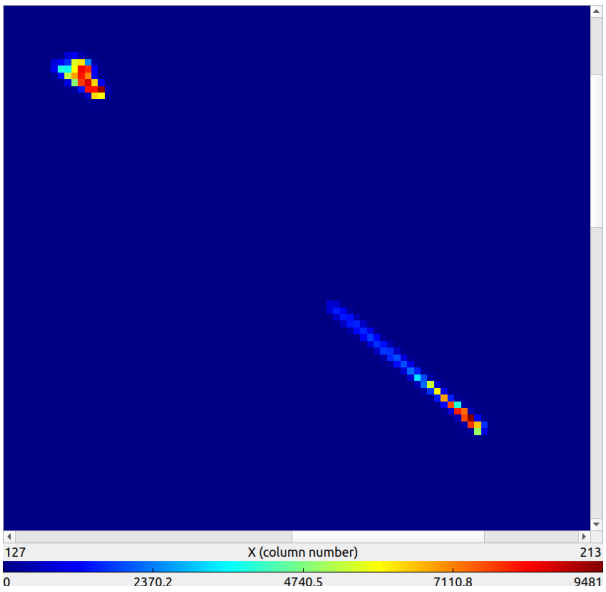

(a) Zoomed in view of the two clusters responsible for the 109 nGy event. Note the maximum energy on the energy scale. Both clusters contain single pixels with energies exceeding 6000 keV.

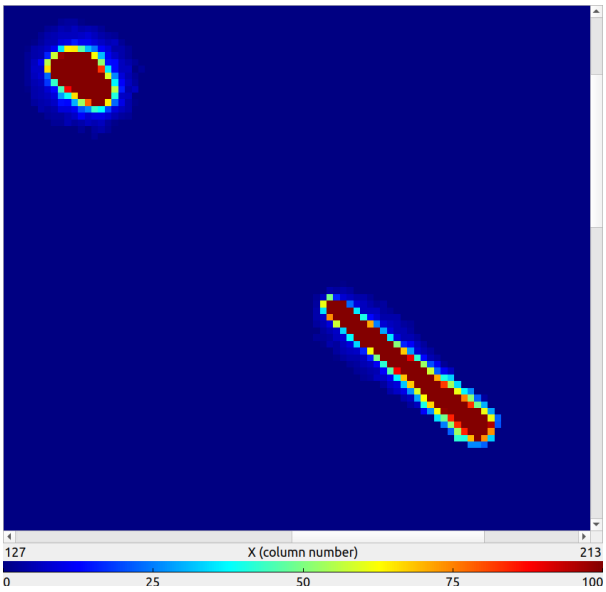

(b) The same image with a reduced energy scale in order to highlight the energy footprint of the clusters.

Figure 3.4.4: MiniPIX data frame showing a 109 nGy event recorded during flight.

3.4.2 Comparison to Previous Missions

During the 2017 and 2018 missions, the MiniPIX was fixed to an aluminum plate which was housed within an ABS plastic structure with dimensions similar to MISS. Figure 3.4.5 presents the dose rates from the 2017 and 2018 UH HASP missions as well as the LET histogram by cluster type from the 2018 data. The 2018 histogram is strikingly similar to the 2019 histogram in terms of the shapes of the counts per cluster type and their relative positioning to one another. An interesting difference between the 2018 histogram and the 2019 histogram is the number of small blobs at lower energies which is much higher in the 2019 data. This is likely due to the increased production of less energetic particles due to the interactions with the MISS structure.

Figure 3.4.5a shows the dose measurements for the 2017 and 2018 missions which were binned in a similar manner to the MISS measurements but with bin widths of 2.5 km. Since the 2017 mission

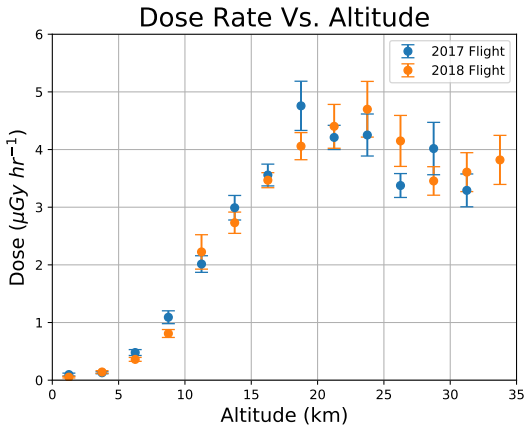

(a) Absorbed dose binned as a function of altitude from the 2017 and 2018 UH HASP missions.

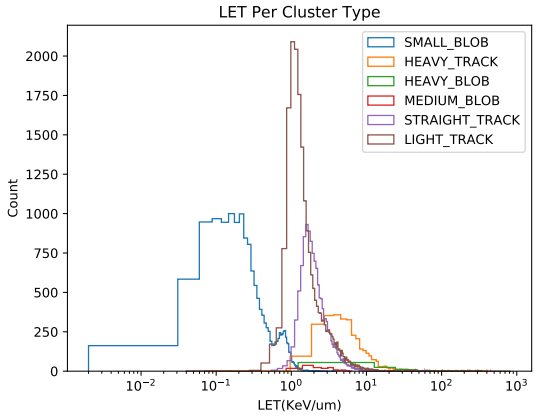

(b) LET histogram of the MiniPIX data from the 2018 UH HASP mission.

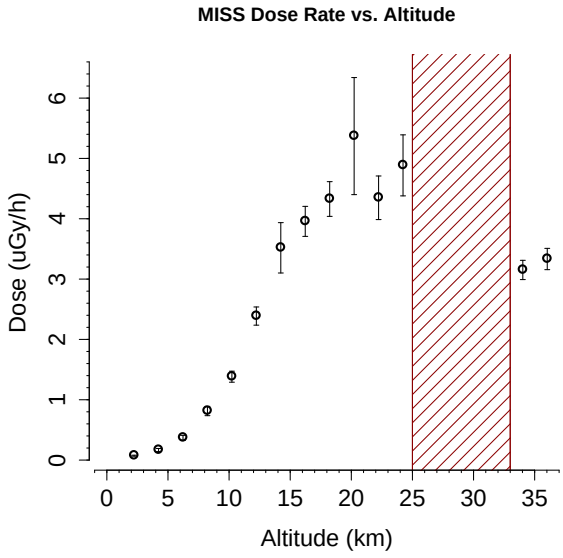

(c) MISS dose versus altitude.

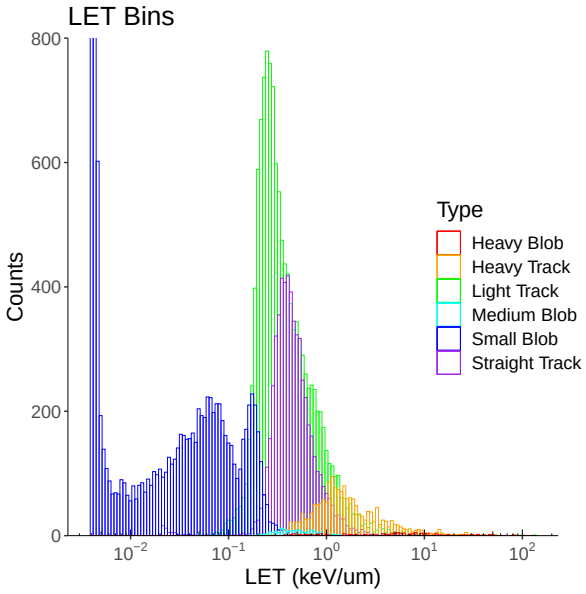

(d) MISS LET spectrum.

Figure 3.4.5: MiniPIX dose rate from the 2017 and 2018 UH HASP missions alongside the LET histogram from the 2018 data. The results from MISS are reproduced for comparison.

used a slightly different measurement methodology for the MiniPIX, the results from MISS will only be compared to those from the 2018 mission, but it is clear that the dose profiles of the 2017 and 2018 missions are very similar to that of 2019. However, at higher altitudes, the average bin values are slightly higher for MISS than those from the 2018 mission. In fact, there is approximately a 16% increase in dose rate from the 2018 mission to the 2019 mission when considering the same

time interval over the 2018 mission, despite the addition of the aluminum shielding in MISS. At least some of this increase is likely due to the solar cycle being closer to its minimum at the time of the 2019 flight, but, considering the tendency for the year-to-year change in GCR intensity to flatten out near solar minimum during even-numbered solar cycles [62], the structure of MISS and its materials may have contributed as well.

3.5 Conclusions on MISS

From a general perspective, MISS was successful in observing the radiation environment at high altitudes with a mock-up ISS structure.

The configuration and analysis of the Medipix data are well established within the context of this experiment, and it has proven to provide accurate measurements in a stratospheric environment. However, the structure of MISS could certainly use improvements if choosing to explore this modeling option further in the future.

3.5.1 Contributions of the Author

Since the HASP project as a whole requires group collaboration, it is important to distinguish and reiterate the contributions made by the author of this thesis and those made by others. The MISS experiment, consisting of its design, construction, and flight control programming, was executed wholly by the author unless otherwise noted. Specifically, the cluster analysis and classification algorithm was not developed by the author and was attributed accordingly. Similarly, the calibration of the MiniPIX was not performed by the author and was attributed accordingly.

3.5.2 Future Missions

Applying Medipix detectors to dosimetric applications is a relatively new area of experimental research and is certainly one that should continue to be pursued. For now, the HASP program as a whole has been suspended, so it is not possible to use as a platform for this purpose.

Improvements can certainly be made to the methodology used for MISS. Perhaps the most important improvement would be to use the exact materials used on the ISS. MISS lacked the Nextel and MLI layers, used a different type of aluminum for the outer layer, and used a different Kevlar grade. The difference in aluminum type and Kevlar grade should only have minimal influence on the radiation field, but the introduction of the Nextel and MLI layers could result in a change of measurements due to the modified radiation field. Additionally, monitoring and maintaining an internal pressure of 1 atm is important for accurate modeling. On the HASP balloon, MISS was rather limited in space since it was a subsystem of a larger payload. It would be worthwhile to construct a model with larger dimensions to accurately model the distance particles must travel in the gaps between the material layers. This would also help with heat management as the chassis of MISS would serve as a better heat sink. Larger dimensions would also make the welding job easier as the tight tolerances of MISS proved to make welding a challenge.

A possible addition to the methodology would be to measure neutrons considering their relevance in atmospheric dosimetry. Another addition could be to measure dose equivalent in real-time by using the proper quality factor conversion or a silicon-to-tissue conversion to determine the biological response to the radiation field at these altitudes. This would push this experiment closer to its goal of accurately monitoring the radiation to which humans are exposed at such altitudes. Lastly, a worthwhile addition would be to expand the number of Medipix devices on the flight. This would allow the possibility of taking measurements at various angles or designating different sensors to measure different variables. The only downside to this expansion would be a considerable increase in cost.

Considering that the majority of the pixel values in each data frame is a zero, a compression algorithm could be used to reduce the storage space used by each frame. While this would not typically be necessary for most scientific balloon flights due to their tendency to be on the scale of a few hours or days, this could prove useful for more permanent configurations. Other improvements to the data storage system would be either to use radiation-hardened electronics or to shield the SD card as a preemptive against single event effects. Again, this would only be practical for longer

duration flights or configurations in more intense radiation fields.

Chapter 4

The FLUKA Multi-Particle Transport Code

This chapter introduces the FLUKA transport code [63] [64] through a short history, details the input for simulations, then describes its use within this work.

4.1 A Brief History of FLUKA

The history of FLUKA begins in the mid-1960s. Johannes Ranft began the development of the first FLUKA codes which were used in evaluating the performance of NaI crystals in hadron calorimeters. While at Leipzig University, Ranft worked with CERN-LAB-II on applying his codes to other radiations studies, primarily the CERN 300 GeV project, and Jorma Routti assisted Ranft with expanding FLUKA to consider protons, neutrons, and pions. After receiving improvement suggestions from various scientists, Ranft had updated his codes to describe inelastic hadron interactions and to sample neutral pions, kaons, and antiprotons by the mid-1970s, marking the end of the first FLUKA generation. At this time, the code could not accurately model other phenomena such as multiple Coulomb scattering, electromagnetic cascades, and low-energy particle transport.

In 1978, Ranft began a complete software reformation with the support of Graham Stevenson,

Klaus Gobel, and Jorma Routti. This second generation consisted of several iterations of the FLUKA code during the 1980s with the goal of making the software more user friendly and more flexible. Some additions to FLUKA were the Cartesian and spherical geometries, dedicated low-energy generators, a quark-chain generator, fluence estimators, and more. This second generation greatly expanded the capabilities of the code which gained a lot of attention.

In the late 1980s, scientists began planning accelerators capable of reaching energies of several TeV. By this time, FLUKA was widely used for examining shielding and radiation damage, and the limitations of the program began surfacing. It could not simulate strong magnetic fields, energy deposition in small volumes, high-energy effects, low-energy neutron interactions, and other phenomena that the new accelerators sought to observe. Alfredo Ferrari and Alberto Fassò established a plan to rebuild FLUKA into a program that could simulate general interactions between particles so as to not limit its potential applications. Ranft continued to support the development of the software. After about six years, the software had become the multi-purpose tool that Ferrari and Fassò envisioned. The code structure was updated to take advantage of recent computational developments such as 64-bit computers, increased memory, and numerical accuracy. These changes resulted in precision within 10^{-10} and minimal errors in conserved quantities (e.g., energy and momentum). In addition, improvements were made to the processing and handling of geometry as boundaries between materials and their layers were precisely calculated no matter their size.

Over the course of several decades, FLUKA underwent a transformation from being an application designed for specific physical studies to one that is a powerful general-purpose tool. It continues to be used to study neutrino physics, cosmic rays, accelerators, synchrotron radiation, radiation damage, dosimetry, calorimetry, and more. A team of scientists continues to add to and improve the software, and the tool itself has a world-wide reputation.

4.2 Flair

Flair [65] is a graphical user interface designed to aid the user in preparing and operating FLUKA. The GUI is shallow enough such that the mechanisms of FLUKA do not become obscured as it simply localizes the different components of FLUKA into organized menus. Its features allow the user to edit FLUKA input, monitor the status of simulations, and process results. The integration of gnuplot enables the user to visualize simulation results without requiring further data processing from the user. Perhaps the strongest characteristic of Flair is that it provides near-instant feedback for user actions. It is capable of error detection in the input and is packaged with an interactive geometry viewer.

4.3 The Simulation Environment

FLUKA is a Monte Carlo simulation code. The general operating principle of Monte Carlo simulations is that long, complex calculations are unnecessary. Rather than precisely calculating each variable, a Monte Carlo simulation is provided parameters and models as input and performs stochastic experiments that obey the provided input and record the specified observables. Monte Carlo simulations are inherently random, but the results obtained from such simulations have shown to be valuable and accurate to experimental observations. This is particularly useful in the context of atmospheric studies since phenomena such as particle air showers are extremely complex and would be nearly impossible to model exactly.

4.3.1 Preparing and Running a Simulation

FLUKA operates with "cards." A card is defined in the input file and contains a keyword (the command name), six floating point values called `WHAT`s, and a character string called a `SDUM`. `WHAT`s and `SDUM`s define the parameters of the card but not all may need to be used. For example, the following command would define the position of a particle beam at the Cartesian point (0, 0, -50): `BEAMPOS 0.0 0.0 -50.0`.

The input will contain several sections, each defining a different aspect of the simulation. The different sections of the input can generally be defined in any order with the exception of certain definitions; however, it is of great benefit to the user and others who may read the input to define the sections in a logical manner. An input file begins with a title and any global definitions. Following the title, the particle beam will be defined with its position and the type(s) of particles the beam will produce. This includes the optional cosmic ray definitions that the user wishes to use, the details of which will be explored in-depth in Section 4.3.3. Following the beam definition, the user will define the geometries of the simulation. The geometry definition is broken into three subsections: the size and location of each geometrical body, the layering of each body with respect to one another, and the material definition for each body. The specifics of the geometries used in the GCR simulations for this work will be detailed in Section 4.3.3. After the geometry is defined, the user will then define the various estimators, a detector type, that will measure the desired variables. There are many estimators available, each able to measure different quantities. The estimators relevant to this thesis are the `SCORE`, `USRTRACK`, and `USRBIN` estimators. The `SCORE` estimator which can record the energy deposition or the star density in a region of geometry (star is a legacy name for inelastic hadron reactions). `USRTRACK` measures fluence averaged over a geometry volume. It is a track-length estimator that estimates fluence as a volume density of collisions weighted by the particle mean free path and outputs a fluence differential energy spectra. The `USRBIN` estimator is perhaps the most robust estimator in this application. It is defined over a volume of space (it does not have to correspond to a geometrical body in the input) which is divided three-dimensionally into equal subvolumes whose count and volume is determined by the bin size. Various quantities can be scored with this estimator, but the quantities of interest are dose and ambient dose equivalent. To calculate ambient dose equivalent, FLUKA measures the particle fluence which is convoluted with fluence-to-dose equivalence conversion coefficients generated by ICRP74 and Pelliccioni [66]. These conversion coefficients were calculated using FLUKA and are now embedded in FLUKA to perform the calculations. The supported particles for this conversion are electrons, kaons, muons, neutrons, photons, pions, positrons, and protons, each with their own supported energy ranges (some as low

at 2.5×10^{-11} GeV or as high as 1.0×10^{4} GeV).

Running FLUKA is rather straightforward. Once FLUKA begins, no interaction is needed from the user, and the simulation continues to completion. One *run* can consist of multiple, statistically independent *cycles*. The run is the event begun by the user to start the simulations and carries out a user-specified number of cycles. A cycle is given a number of particle histories (defined in the input file) which is simply the number of primary particles fed into the simulation. Each cycle will have an output file for each estimator defined in the input. Defining a run to have multiple cycles primarily serves as a convenience for the user as the user is able to simulate the input through multiple iterations without needing to constantly restart the FLUKA program. The data generated by each cycle is localized and indexed which aids with post-processing.

4.3.2 Post-Processing

FLUKA is shipped with several Fortran utility scripts that handle post-processing the simulation results. There is a different script for each of the different estimators, but each script is functionally the same. The user provides the data files to be examined, and the script will combine all of the provided files into one dataset. This output dataset may be stored in multiple representations, but it is generally either in a binary format or a human-readable, tabulated format. The combined dataset is statistically equivalent to the sum of the individual datasets used to generate it, and errors are associate with each measurement.

Most of the data visualization was performed with gnuplot in Flair. A simple Python script was used to interface with the dose measurements of the `USRBIN` dose estimator. The script summed the measurements into one quantity for each altitude so that the results could be directly compared to those of MISS.

4.3.3 GCR Calculations

GCR calculations can be performed using FLUKA. The `GCR-SPE` card initializes a GCR source which can be configured to the user's liking through specifying the desired GCR spectra. FLUKA

contains data files that define the GCR spectra at solar minimum and at solar maximum for each atom from atomic number 1 to 28. The spectra were derived from Badhwar and O'Neill's GCR radiation model defined in Ref. [67] and improved using datasets from the Alpha Magnetic Spectrometer (AMS) and the Balloon-borne Experiment with a Superconducting Spectrometer (BESS). For this thesis, the spectra at solar minimum were chosen since the HASP flight at about the same time as the solar minimum at the end of Solar Cycle 24.

FLUKA features an original algorithm to treat multiple Coulomb scattering and the transport of charged particles. This approach has been shown to accurately model complex phenomena such as electron back-scattering and energy deposition in thin layers [68]. For nuclear interactions, the `PEANUT` package is used for energies below 5 GeV/nucleon which uses a generalized intra-nuclear cascade model [69]. When considering GCRs, the `DPMJET-II.5` interaction model was chosen to simulate nucleus-nucleus collisions above 5 GeV/nucleon which allows the simulation of particles up to 500 TeV.

4.4 Input Geometry and the Timepix

4.4.1 The Earth Model

The FLUKA installation includes an auxiliary Fortran program that can generate geometry for GCR-related simulations. The script is given geographic coordinates on the Earth, altitude, and energy cut-offs and outputs a geometry file that includes a full-scale Earth with its atmosphere sectioned into 100 concentric spheres. The Earth is given a radius of 6378.1 km and the outermost atmospheric layer a radius of 6449.7 km. It also produces an auxiliary file that defines the geomagnetic coordinates of the Earth's magnetic field relative to the specified geographic location as well as various scoring parameters used at runtime. A separate, general materials file defines the gas mixture composition (of nitrogen, oxygen, and argon) and air pressure for each atmospheric layer in accordance with the U.S. Standard Atmosphere density profile. The Earth geometry uses intersecting cones to render only the environment around the specified coordinates. This Earth

model was not used for performing the actual simulations.Reasoning for not using the Earth model can be justified by the fact that the scale of the Earth geometry is simply too large in comparison to the MISS geometry. Tests using this spherical geometry resulted in a lack of useful measurements recorded by MISS due to the very small probability of a particle coming into contact with the structure. Increasing the probability of incidence would require a much larger number of simulated primary particles, but this is impractical as the required number of primaries would drastically increase the computation time to limits ill-placed within the context of this thesis.

Instead of the spherical Earth geometry, a flat Earth geometry was used. In general, a flat geometry is preferred for calculations concerning dose and atmospheric depth since these calculations are insensitive to the curvature [70] [71] [72]. FLUKA does not contain a program that can generate a flat Earth geometry, so a geometry was created for this work. The atmosphere was constructed using the same 100 layers and air compositions generated by FLUKA's auxiliary file, but, rather than being concentric spheres, the layers were stacked rectangular prisms with 750 m by 750 m cross-sections and thicknesses matching the spherical geometry. The entire geometry was surrounded by a black hole. Black holes in FLUKA serve to dispose of any particles that were either never relevant or are no longer relevant to the simulation. Examples of such particles would be particles that have either completely missed the MISS geometry or the particles that have already interacted with the geometry. The flat Earth geometry has several advantages over the spherical geometry. The first is that the computation time is much lower which in turn allows for an increased number of primaries to be simulated. The second is that managing the geometry and the placement of MISS within the atmosphere is easier. The third is that the GCR source is now a point source. FLUKA only allows two GCR source configurations that are suitable for this kind of application. One option is to define a radius at which GCRs are generated (this is the definition for the spherical Earth), and the other option is to choose a point in space at which the GCRs are isotropically produced (this is the definition for the flat Earth). At first, this may seem odd, but it has the benefit of saving computation time since all primaries that would not subsequently result in an interaction with MISS are almost immediately discarded into the black hole. Lastly, the energy

range for the generated primary particles was skewed towards higher energies with a minimum energy of 3 GeV. Doing so resulted in a trade-off of sacrificing the lower energy primaries, which may not result in subsequent particle interactions with the MISS structure, and allowing higher energy primaries, which would result in more interactions with MISS. This allowed for more time spent on computing higher energy particles and higher energy air showers.

The auxiliary program mentioned previously was used to model the atmospheric and geomagnetic conditions around the balloon's launch location. The chosen coordinates were 34°N 104°W, which is the geographic coordinate of Fort Sumner, New Mexico. Since the balloon flight was only a few hours in duration, the balloon had only drifted about 610 km to 37.5°N 109.9°W. This change in geographic position is not significant, so the auxiliary files generated for Fort Sumner's coordinates were used for all simulations. This is a safe assumption to make as the air composition would be consistent across the atmosphere, and the geomagnetic rigidity does not greatly vary with minor changes in geographic position at lower latitudes [73].

4.4.2 The MISS Model

The geometry of MISS was modeled almost exactly like the structure that flew on the HASP balloon in terms of the ISS structure. Since the assumption that the airtight seal did not hold during the balloon launch, the empty space between each of the solid layers was assigned the same air composition as the atmospheric layer in which MISS was in at each particular altitude. Not included in the FLUKA geometry was the USB interface for MISS and the plastic housing the MiniPIX's readout electronics. Additionally, the lengths and widths of each layer were increased by a factor of 1000, but the thicknesses of each layer were kept the same. This was done in order to increase the cross-section which in turn increases the number of interactions with the MISS model by a proportionate amount. It is reasonable to assume that this proportion is kept constant at each atmospheric layer since the diameter of the particle footprint for air showers is usually on the order of hundreds to thousands of meters [1] [74]. The thicknesses of the materials were kept the same in order to accurately model the distance of particle propagation through the structure. The

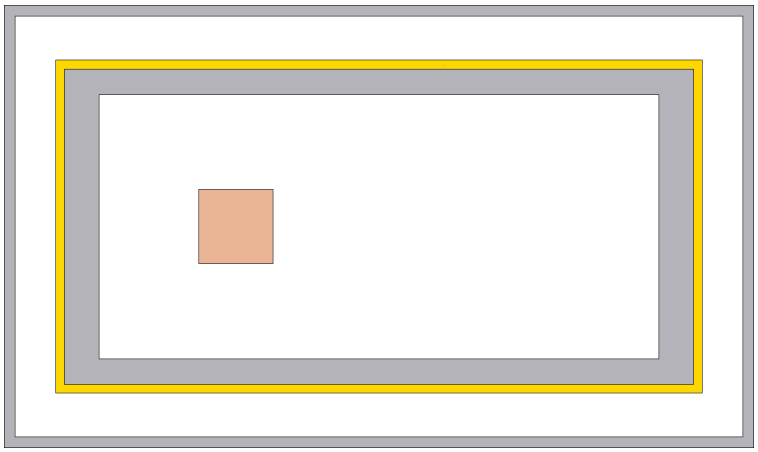

Figure 4.4.1: Image depicting MISS within FLUKA. The layers, as previously defined, are clearly shown along with the Timepix sensor in the inner-most region. The white regions, which depict empty space, were given the same gaseous composition as the atmospheric layer within MISS resided for each particular altitude.

cross-section of MISS, as generated by FLUKA, is shown in Figure 4.4.1

Since Kevlar is not a FLUKA-defined material, it was defined by building a molecular compound using FLUKA's `COMPOUND` card which defines the composition of the compound in terms of its atoms, and the density was specified as $1.44\,\mathrm{g\,cm^{-3}}$. Thirty simulation runs each consisting of five cycles each with 20 000 000 primary particles were performed. For each simulation run, MISS was set to a different altitude resulting in measurements at altitudes from 1 km to 30 km with roughly equal spacing.

A `USRBIN` estimator was defined as an array of 256 by 256 bins in the x-y plane with 1 bin in the z direction where the z direction is perpendicular to the surface of the Earth. The estimator had dimensions of 1.408 cm by 1.408 cm by 0.03 cm matching that of the silicon sensor of the MiniPIX. This bin structure emulates the pixel array structure in the Medipix sensor, and the structure of the data output from this estimator is comparable to that of the MiniPIX. As shown in Figure 4.4.2, a plot of the binned dose measurements results in an image resembling a data frame from the MiniPIX.

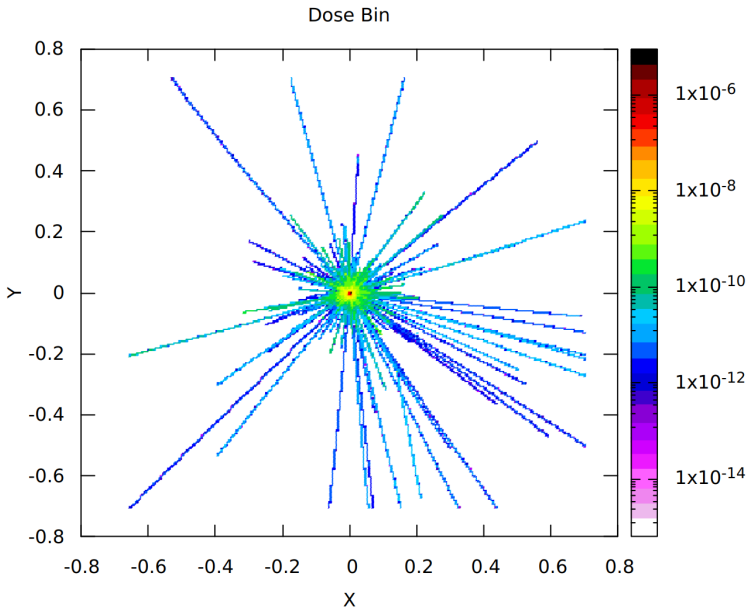

Figure 4.4.2: Example of a plot featuring `USRBIN` data from an example simulation in which a proton beam was shot at a thin silicon target.

4.4.3 Simulation Benchmarking

Prior to performing the simulations for this thesis, a benchmark was conducted which compared FLUKA results to experimental data to ensure the FLUKA environment was properly configured. The benchmark simulation used an Earth geometry generated by FLUKA's auxiliary program and the GCR simulation template. Five simulation cycles each generated 100 000 primary particles outside of the outermost atmospheric layer and the specified estimators recorded the results. The measured quantities were the primary particle fluence at the top of the atmosphere and the μ^+ and μ^- fluence at the Earth's surface; the results of which are shown in Figure 4.4.3. The results of the benchmark are comparable to the experimental results measured by Ref. [75] and Ref. [76].

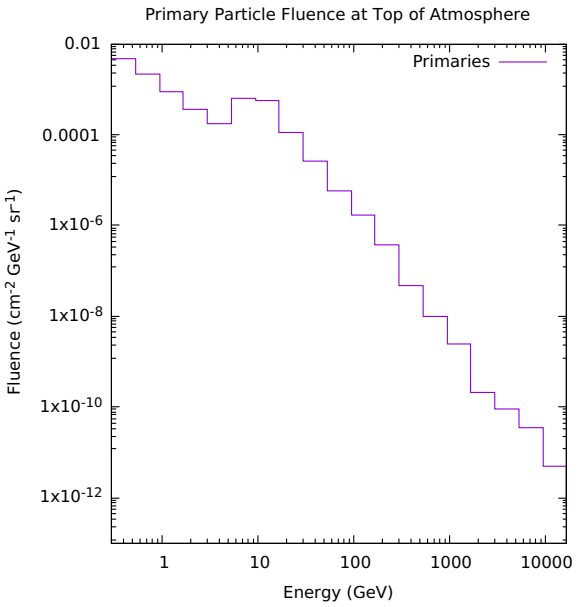

(a) Primary particle fluence at the top of the Earth's atmosphere during benchmark tests.

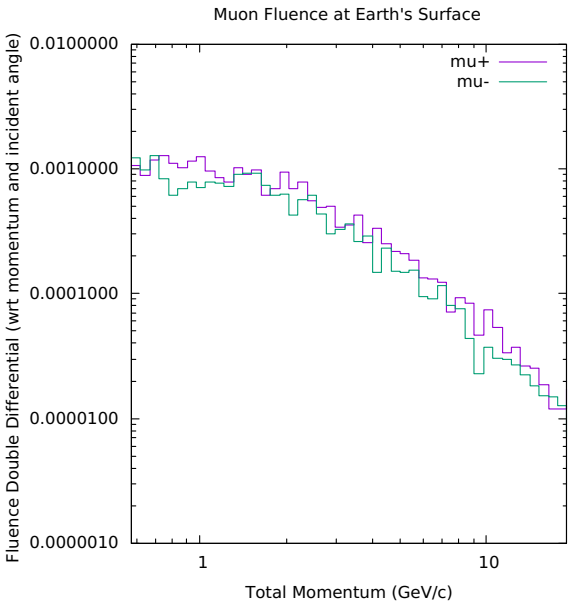

(b) μ^+ and μ^- fluence at the surface of the Earth during benchmark tests.

Figure 4.4.3: FLUKA benchmark results using its standard GCR models at solar minimum.

4.5 Simulation Results

The results from the simulations follow the general trend as those obtained during the balloon flight. As seen in Figure 4.5.1, the Regener-Pfotzer maximum is accentuated, likely due to the approximations to the model, the energy range set for the primary particles, and the number of primary particles generated for each run. The dose scale is not particularly relevant due to the method with which FLUKA calculates and reports the dose. The dose is calculated with fluence-to-dose conversion parameters and normalized to the detector volume. Since this internal scaling in FLUKA is constant for each run, the important feature of the plot is the relative shape of the curve.

While the dose results from the simulations do not closely match the results from MISS, they do share similarities to the results total ionizing dose (TID) detector flown as part of NASA's RaD-X missions which will be explored more in-depth in Section 4.6 [6].

The consequence of setting the minimum primary energy to 3 GeV can be seen in the spectra

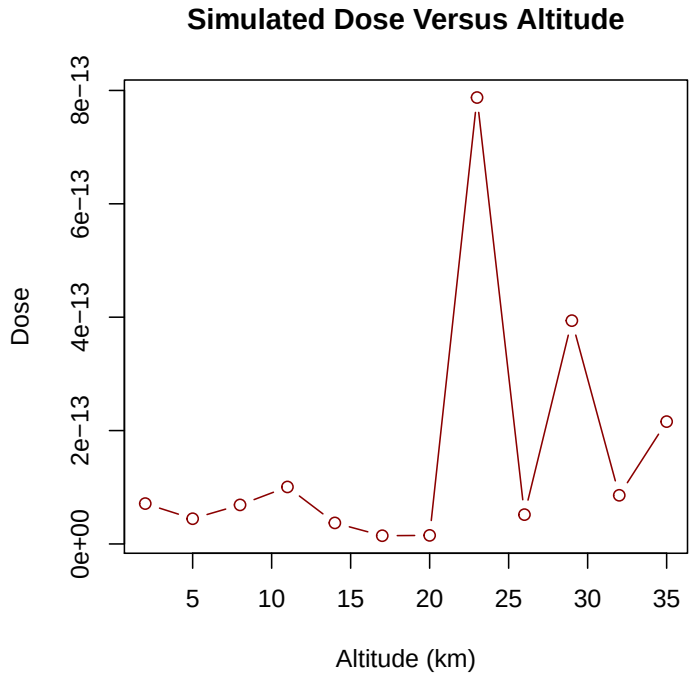

Figure 4.5.1: Dose measurements made by the FLUKA simulations. The results were put into 3 km wide bins similar to the dose measurements made by MISS during the balloon flight.

presented in Figure 4.5.2. The primary particle fluence, shown in Figure 4.5.2a, resembles the fluence spectrum obtained during the benchmark tests except now the fluence spectrum begins at 3 GeV, as defined. Figure 4.5.2b shows the surface muon fluence, and the influence on the surface muon count is more noticeable, as there is a reduction in the number of lower energy muons.

The LET spectra were scored at each altitude, however, their quantities and statistical uncertainty were indicative of a low sample size. Due to the large uncertainty in these values, the simulated quantities were not compared to the LET obtained by MISS. To improve on this, a larger number of particles would need to interact with the silicon sensor.

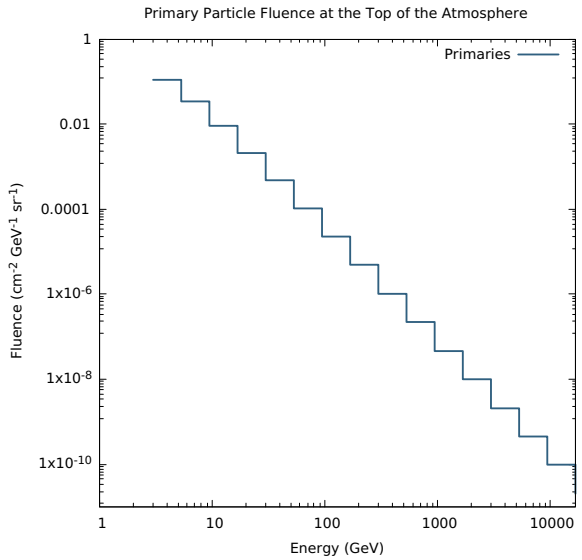

(a) Primary particle fluence at the top of the Earth's atmosphere.

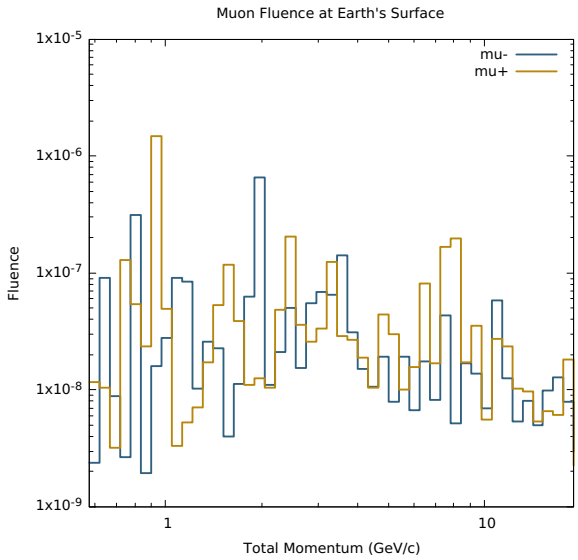

(b) μ^+ and μ^- fluence at the surface of the Earth.

Figure 4.5.2: Fluences obtained from the simulation configuration. These are the results from one simulation run, but all 36 runs shared similar results for these variables.

4.6 Discussion and Works Performed by Others

The results of the FLUKA simulations are discussed with the MISS observations, and, to supplement the results obtained from the simulations, work from other scientists regarding this topic is presented.

An attempt at further processing the FLUKA data was made by considering the time spent by the HASP balloon in each altitude range. Since the same number of primaries was used in each simulation run, the idea was to normalize the simulated dose against the relative time duration in each altitude range. It was found that the HASP balloon traveled vertically at roughly the same speed for the duration of its ascent, so the effect of this scaling on the FLUKA data was not included since it was small and not notable.

The NASA Radiation Dosimetry Experiment (RaD-X) featured various dosimeters aboard stratospheric balloon flights with the goal of obtaining a better understanding of cosmic radiation in the atmosphere and human exposure to radiation in aviation environments. The balloon

flew a diverse collection of dosimeters which included a Teledyne TID detector, a silicon-based, thumb-sized dosimeter. In terms of shape and prior to data filtering techniques, the TID yielded dose rates comparable to those obtained from the FLUKA simulations performed as part of this work. A filter is applied to the TID data to remove statistical fluctuations and results in a smooth curve comparable to the one obtained by MISS. Due to the relatively small sample size, a similar filter on the simulation data was not performed. Aside from the dip to near-zero at about 28 km, the trend of the simulations follows the TID results. Additionally, the dose rates recorded by all RaD-X instruments are comparable to those obtained during the HASP missions, and, in making this comparison, it is important to note that the RaD-X flight took place in 2015. The plot from the RaD-X results is shown in Figure 4.6.1. While not shown in this thesis, it is worth mentioning that RaD-X also reports dose equivalent values which provide a better insight into the biological risk at these altitudes. An interesting observation made by RaD-X is that the dose equivalent does not peak as the absorbed dose does. In fact, the dose equivalent reaches a maximum at the Regener-Pfotzer maximum and maintains that value through higher altitudes.

Considering the relative similarity of the dose profile from MISS to the dose profile observed without a surrounding structure, it is worthwhile to compare the results from MISS to FLUKA simulations performed by others which explore the dose in the atmosphere. Perhaps the most notable is the aircrew exposure study performed by Ferrari et al. [77]. In this study, FLUKA was used to model an Airbus 340 containing passengers to observe the effect the aircraft's structure has on the radiation field at aviation altitudes. It was found that the effect was not negligible, and the resulting net ambient dose equivalent was lower than in the free atmosphere. Since neutrons are very relevant within the context of aircraft, it important to note that this model considered the particle interactions with the aircraft's fuel as well. As part of a future work, a similar methodology of comparing the ratio of dose in the structure with respect to the dose in the free atmosphere could be used with the simulation doses in the MISS structure in order to obtain a better understanding of the structure's influence on the radiation field.

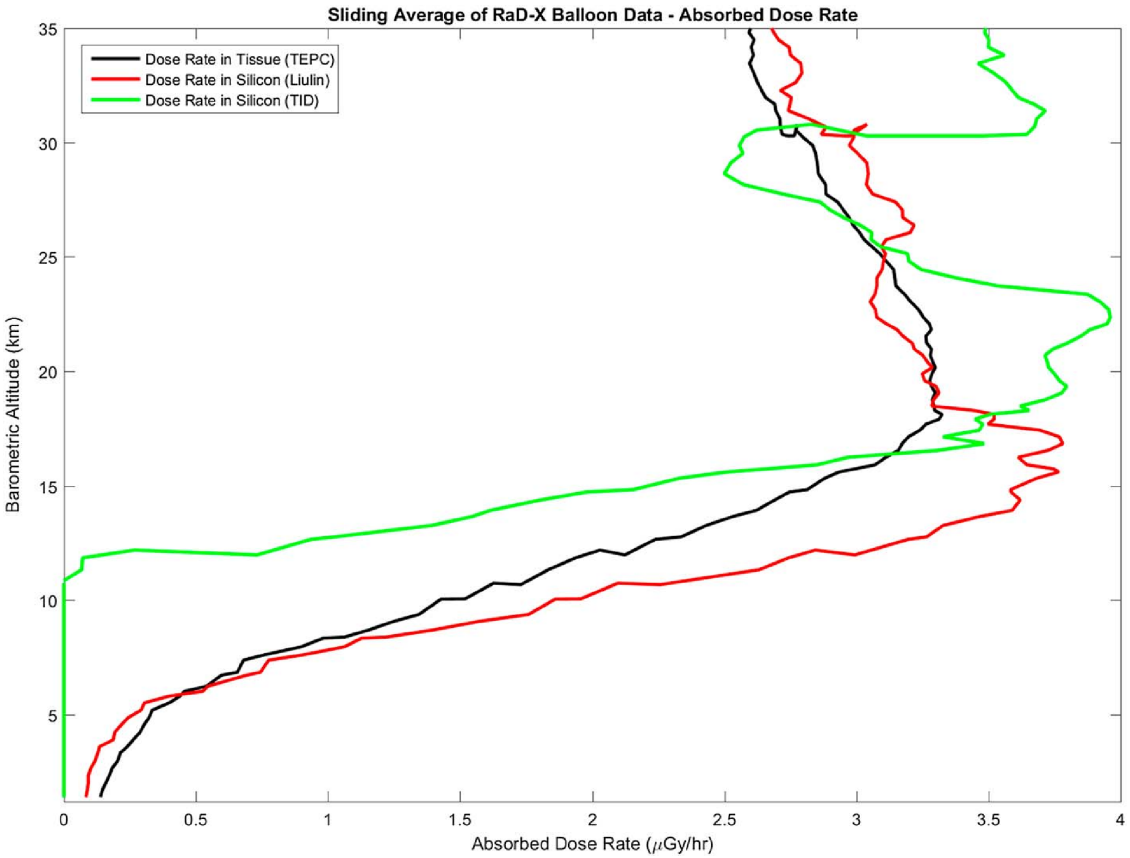

Figure 4.6.1: Results from the RaD-X campaign prior to the application of filtering techniques, as presented in Ref. [6]. The TID results are shown in green.

4.7 Conclusions on the FLUKA Study

Aside from the presence of the Regener-Pfotzer maximum, the results from the simulations did not closely match the dose profile obtained by the MiniPIX, but they did share strong similarities to the TID sensor used in the NASA RaD-X mission.

While the simulations yielded meaningful results, they were rather narrow and could see expansion in terms of the number of observables recorded. Additionally, the geometries could certainly be improved. The atmosphere geometry only allows consideration of particles which are perpendicular to the Earth's surface, and the full width of each air shower is not considered due to the limited cross-section of the atmosphere's layers. This geometry configuration and the lower limit

set for the primary particles had a non-negligible effect on the simulation results, as seen in the resulting muon fluence on the Earth's surface. Both of these limitations were set in order to reduce the computation time, but this could be accommodated using different hardware or an extended period of time. Doing so would produce more accurate dose, LET, and fluence measurements as well as a more comprehensive view of the interactions with the structure. Furthermore, a higher resolution could be obtained for the dose profile by decreasing the altitude increment between each simulation. Since simulations were performed at 1 km increments, there were 36 runs performed for this study.

It would also be worth exploring this study using other simulation toolkits. Several parameters used by FLUKA, such as the fluence-to-dose conversion values, were calculated using data simulated by FLUKA. Leaving the FLUKA environment and using a different toolkit could yield different results which may highlight a characteristic of the MISS configuration which cannot be seen solely through FLUKA.

Chapter 5

Conclusions

Dosimetric applications of Medipix sensors have proven to be a venture worth exploring and developing. The accuracy of the sensors and the plug-and-play nature of the electronic interface of devices such as the MiniPIX results in a very reliable, robust system that can be adapted to be remotely configured and transmit data in real-time. Such systems are necessary as human activity above the Earth's surface and outside of its atmosphere continues to expand.

The MISS experiment proved to be successful in making measurements in the stratosphere, and the methodology used to develop MISS is robust enough to allow either an easy expansion of the experiment or a transfer towards other applications. While the experiment had its successes in its measurements of the dose profile through the atmosphere as well as the LET spectra measurements in the mixed radiation environment, there are certain aspects that could see improvement. In particular, the construction materials and the size of the structure certainly limited the accuracy of the model. Furthermore, the HASP program, while certainly a well-executed and high-quality platform, is not well-suited to allow for such improvements considering the space limitation for each student payload. Other balloon programs could be used to accommodate such a device, but a more constructive approach would be to focus on the development of a miniature aviation model which could compare directly to measurements made aboard aircraft as well as dosimetry simulations of aircraft, such as the study performed by Ferrari et al. [77].

As for the simulations, the experiment was modeled in FLUKA with MISS and a flat Earth geometry with some approximations. A lower limit of 3 GeV was set for the primary particle energy, and the cross-section of the atmosphere was 750 m by 750 m. An analysis of the surface muons reveals the impact of the approximations, as the number of recorded lower energy muons is considerably smaller than those recorded with less severe approximations. The dose profile obtained through FLUKA did not closely match that of the MISS experiment, but its trend is comparable to results recorded by a silicon sensor from the RaD-X balloon campaign prior to the application of a filtering technique. By performing a larger number of simulations and by reducing the approximations made in this study, more accurate results would follow and would allow for a more detailed analysis.

5.1 Future Work

The work of this thesis is easily expandable considering the aforementioned increasing relevance of space weather.

The suggestion of a push towards accurate, detector-based monitoring of aviation radiation is certainly more of a long-term goal in the scope of this experiment. This experiment used detector data compared to that of simulation data and data from others in order to legitimize the methodology used in the detector experiments, but the purpose is not necessarily to compare the *accuracy* but the *precision* of the mock-up model to the computational models and the experiments of others. By further developing this monitoring system to accommodate additional Medipix devices or to measure additional variables such as dose equivalent or neutron presence, the result would be a compact, accurate, robust, and relatively cheap radiation dosimeter.

If possible, the next step towards reaching the long-term goal could one of two options. The first would be to continue the development of a mock-up ISS model with the intent of modeling and predicting the dosimetric environment of the actual ISS. A future iteration with the proper material model at a higher altitude could have a chance of achieving this. Alternatively, one could

abandon the use of atmospheric balloon flights and move to a lab environment similar to CERF. In this case, the data gathered by the physical model could be compared against simulations as well as data from the actual ISS. While this removes the in-situ nature of the experiment (which was one of the main motivators of this work), a successful model of the ISS could be generalized and applied to modeling more exotic environments such as the Moon or Mars.

The second is the more attractive option as it would be more practical in terms of civilian safety and could potentially prove to provide reliable active monitoring for commercial airline crews. This option would be to construct a mock-up airplane model in a similar fashion to MISS. The model would need to be larger than MISS in order to accommodate the thick chassis of commercial planes as well as a compartment containing fuel. For this structure, the fuel would be crucial to model considering the thermal neutron production due to interactions between the fuel and the high energy neutrons produced by cosmic rays in the atmosphere [78]. This model could either be flown on an atmospheric balloon or used in a lab such as CERF and could perhaps be used to study the effectiveness of a mock-up model compared to the actual environment. Ideally, similarities would be seen when comparing the data, highlighting the ease by which a real-world application can be designed to accurately replicate the space-like environments in which humans currently reside, and decreasing the high dependence on computational models. Nevertheless, if either route is successful, such miniature models could have applications in replacing or supplementing the use of computational simulations.

Improvements in the simulations would generally follow in line with what was described for the improvements and changes for the physical models. Additional improvements would include more accurate modeling of the atmosphere by increasing the cross-section of the layers to account for angled particles, increasing the number of primary particles used in each cycle, and widening the range for primary particle energies. Further development would include measuring doses at both solar maximum and solar minimum, performing a detailed analysis of the particle species which interact with the silicon sensor, and exploring additional simulation toolkits (e.g., Geant4) for modeling this configuration.

Of course, the most prudent approach would be to establish active monitoring systems aboard actual commercial airplanes. Considering the already high expense of constructing and maintaining such airplanes, using a Timepix device for this purpose would, comparably, be a negligible monetary cost. An approach such as this would decrease the high dependence on computational models for measuring aircrew exposures to radiation.

Appendix A

MISS Detailed Specifications

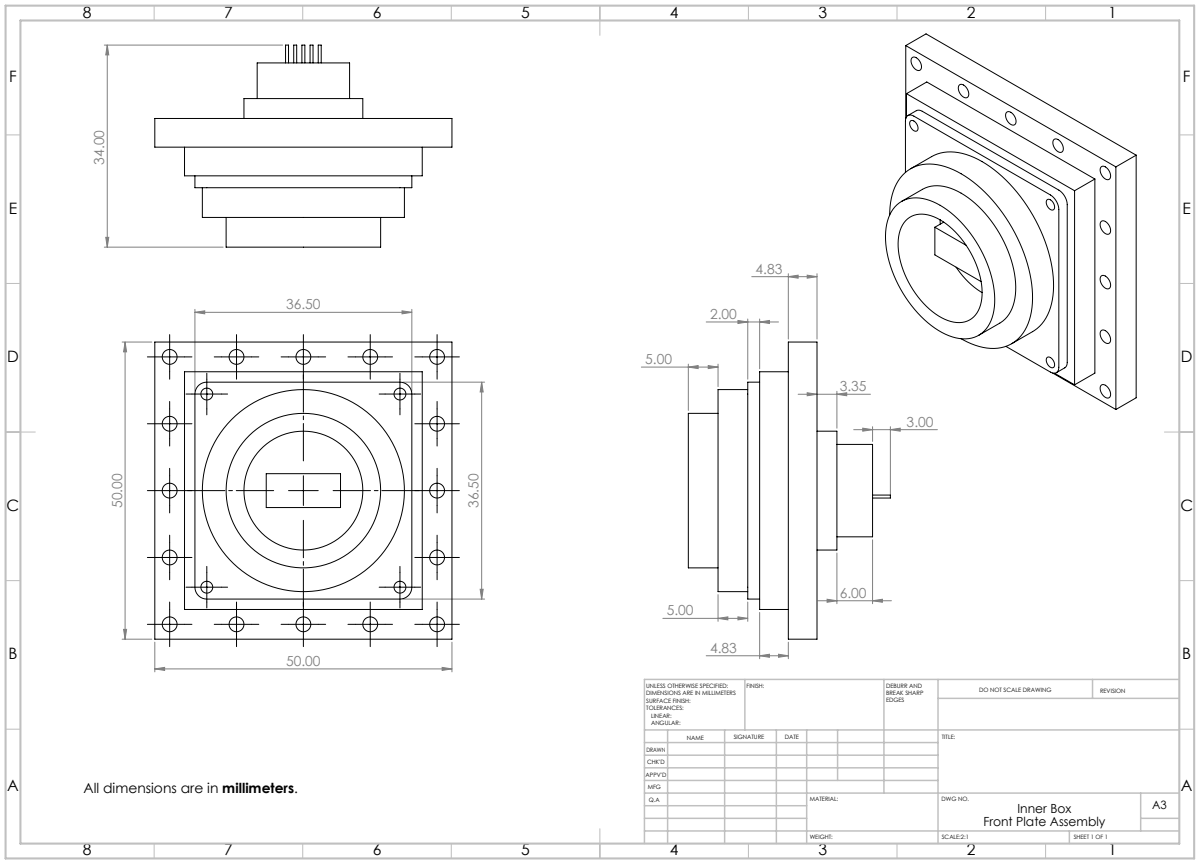

Figure A.0.1: A detailed view of the front panel construction for MISS.

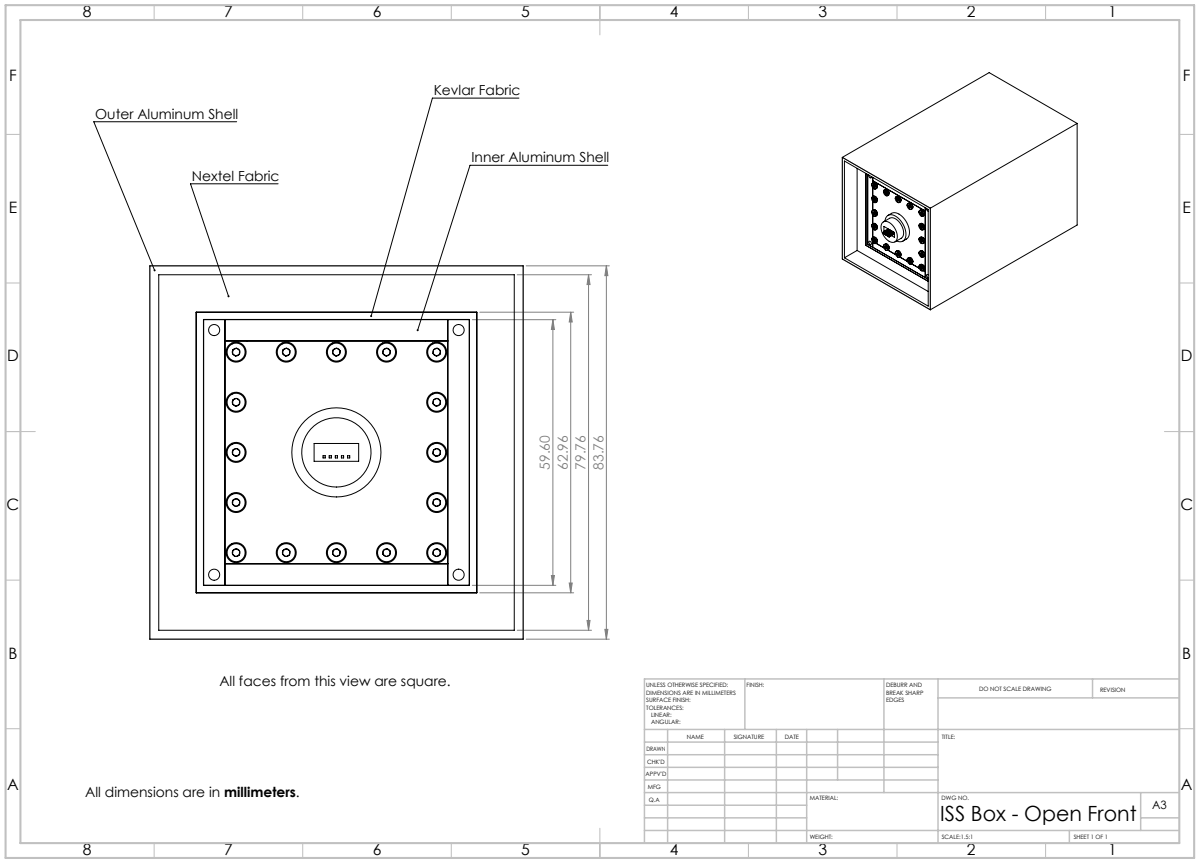

Figure A.0.2: A detailed front view of MISS with the front plate removed.

Appendix B

Medipix Metadata

Listing B.1: MiniPIX Metadata Example

```
[F42]
Type=i16 matrix width=256 height=256
"Acq Serie Index" ("Acquisition serie index"):
u32[1]
0
"Acq Serie Start time" ("Acquisition serie start time"):
double[1]
1566594431.445231
"Acq time" ("Acquisition time [s]"):
double[1]
1.000000
"ChipboardID" ("Chipboard ID"):
char[9]
H06-W0239
"DACs" ("DACs"):
u16[14]
1 100 225 127 127 0 712 8 130 158 80 85 128 128
"HV" ("High voltage [V]"):
double[1]
```

```
200.000000
"Interface" ("Readout interface"):
char[7]
MiniPIX
"Mpx type" ("Medipix type (1-MXR, 2-TPX, 3-MPX3, 4-TPX3)"):
i32[1]
2
"Pixet version" ("Pixet version"):
char[5]
1.4.7
"Start time" ("Acquisition start time"):
double[1]
1566594432.488327
"Start time (string)" ("Acquisition start time (string)"):
char[64]
Fri Aug 23 21:07:12.488327 2019
"Threshold" ("Threshold [keV]"):
double[1]
57.684538
"Timepix clock" ("Timepix clock"):
double[1]
10.285714
"Timepix mode" ("Timepix mode (0-Medipix,1-ToT,2-1Hit,3-Timepix)"):
byte[1]
1
```

Bibliography

[1] F. G. Schröder, "Radio detection of cosmic-ray air showers and high-energy neutrinos," *Progress in Particle and Nuclear Physics*, vol. 93, p. 1–68, Mar 2017.

[2] N. A. Schwadron, J. B. Blake, A. W. Case, C. J. Joyce, J. Kasper, J. Mazur, N. Petro, M. Quinn, J. A. Porter, C. W. Smith, S. Smith, H. E. Spence, L. W. Townsend, R. Turner, J. K. Wilson, and C. Zeitlin, "Does the worsening galactic cosmic radiation environment observed by crater preclude future manned deep space exploration?," *Space Weather*, vol. 12, no. 11, pp. 622–632, 2014.

[3] U. Nations, *Sources and effects of ionizing radiation: United Nations Scientific Committee on the Effects of Atomic Radiation : UNSCEAR 2000 report to the General Assembly, with scientific annexes*. United Nations, 2000.

[4] S. George, *Dosimetric Applications of Hybrid Pixel Detectors*. PhD thesis, University of Wollongong, 2015.

[5] E. Christiansen and D. Lear, "Micrometeoroid and orbital debris environment & hypervelocity shields." NASA Presentation, February 2012.

[6] C. J. Mertens, G. P. Gronoff, R. B. Norman, B. M. Hayes, T. C. Lusby, T. Straume, W. K. Tobiska, A. Hands, K. Ryden, E. Benton, *et al.*, "Cosmic radiation dose measurements from the rad-x flight campaign," *Space Weather*, vol. 14, no. 10, pp. 874–898, 2016.

[7] N. Artemis. Found at `https://www.nasa.gov/artemis`.

[8] M. Garcia, "International space station facts and figures," 2019.

[9] M. Lemoine and G. Sigl, "Physics and astrophysics of ultra-high-energy cosmic rays," in *Physics and Astrophysics of Ultra-High-Energy Cosmic Rays*, Lecture notes in physics, 576., (Berlin ;), Springer, 2001.

[10] Blasi, Pasquale, "Galactic cosmic rays," *EPJ Web of Conferences*, vol. 105, p. 00002, 2015.

[11] J. Alvarez-Muñiz, M. Risse, G. Rubtsov, and B. Stokes, "Review of the multimessenger working group at uhecr-2012," *EPJ Web of Conferences*, vol. 53, p. 01009, 2013.

[12] S. Funk, "Ground- and space-based gamma-ray astronomy," *Annual Review of Nuclear and Particle Science*, vol. 65, no. 1, pp. 245–277, 2015.

[13] B. W. Carroll and D. A. Ostlie, *An Introduction to Modern Astrophysics*. Pearson Addison-Wesley, 2014.

[14] U. Tortermpun, D. Ruffolo, and J. W. Bieber, "Galactic cosmic-ray anistropy during the forbush decrease starting 2013 april 13," *The Astrophysical Journal*, vol. 852, p. L26, Jan 2018.

[15] R. U. Abbasi, M. Abe, T. Abu-Zayyad, M. Allen, and et. al., "Depth of ultra high energy cosmic ray induced air shower maxima measured by the telescope array black rock and long ridge fadc fluorescence detectors and surface array in hybrid mode," *The Astrophysical Journal*, vol. 858, no. 2, p. 27, 2018-05-10.

[16] J. Bellido, "Measurement of the average depth of shower maximum and its fluctuations with the pierre auger observatory." 31st Internat.Cosmic Ray Conf., Lodz, PL, July 7-15, 2009 Proc.on CD-ROM Paper 0124 Lodz : University of Lodz, 2009, 2009. 51.53.01; LK 02.

[17] E. Regener and G. Pfotzer, "Vertical intensity of cosmic rays by threefold coincidences in the stratosphere," *Nature*, vol. 136, pp. 718–719, 1935.

[18] R. Sarkar, S. K. Chakrabarti, P. S. Pal, D. Bhowmick, and A. Bhattacharya, "Measurement of secondary cosmic ray intensity at regener-pfotzer height using low-cost weather balloons and its correlation with solar activity," *Advances in Space Research*, vol. 60, no. 5, pp. 991–998, 2017-09-01.

[19] A. D. P. Hands, K. A. Ryden, and C. J. Mertens, "The disappearance of the pfotzer-regener maximum in dose equivalent measurements in the stratosphere," *Space Weather*, vol. 14, no. 10, pp. 776,785, 2016-10.

[20] C. J. Mertens, "Overview of the radiation dosimetry experiment (rad-x) flight mission," *Space Weather*, vol. 14, no. 11, pp. 921–934, 2016.

[21] A. Nelles, S. Buitink, A. Corstanje, J. E. Enriquez, H. Falcke, J. R. Hörandel, J. P. Rachen, P. Schellart, O. Scholten, S. ter Veen, S. Thoudam, and T. N. G. Trinh, "A new way of air shower detection: measuring the properties of cosmic rays with lofar," *Journal Of Physics, Conference Series*, vol. 632, no. 1, pp. 1,11, 2015.

[22] P. Auger, A. Aab, P. Abreu, M. Aglietta, and et. al., "The pierre auger cosmic ray observatory," *Nuclear Instruments and Methods in Physics Research A*, 2015.

[23] G. Dubus, J. Contreras, S. Funk, Y. Gallant, T. Hassan, J. Hinton, Y. Inoue, J. Knödlseder, P. Martin, N. Mirabal, M. de Naurois, and M. Renaud, "Surveys with the cherenkov telescope array," *Astroparticle Physics*, vol. 43, no. C, pp. 317 – 330, 2013-03.

[24] W. Apel, J. Arteaga-Velázquez, K. Bekk, M. Bertaina, and et. al., "Kascade-grande measurements of energy spectra for elemental groups of cosmic rays," *Astroparticle Physics*, vol. 47, no. C, pp. 54,66, 2013-07.

[25] ICRP, "1990 Recommendations of the International Commission on Radiological Protection. ICRP Publication 60," *ICRP*, pp. 1–221, 1990.

[26] B. Grajewski, E. A. Whelan, C. C. Lawson, M. J. Hein, M. A. Waters, J. L. Anderson, L. A. MacDonald, C. J. Mertens, C.-Y. Tseng, R. T. Cassinelli, *et al.*, "Miscarriage among flight attendants," *Epidemiology (Cambridge, Mass.)*, vol. 26, no. 2, p. 192, 2015.

[27] N. C. on Radiation Protection and Measurements, "National council on radiation protection and measurements: Ionizing radiation exposure of the population of the United States," *Radiation Protection Dosimetry*, 2009.

[28] NASA, "NASA space flight human-system standard volume 1 revision a: Crew health," tech. rep., United States of America, 2007.

[29] G. Reitz, T. Berger, and D. Matthiae, "Radiation exposure in the moon environment," *Planetary and Space Science*, vol. 74, no. 1, pp. 78–83, 2012.

[30] D. M. Hassler, C. Zeitlin, and R. F. e. a. Wimmer-Schweingruber, "Mars' surface radiation environment measured with the mars science laboratory's curiosity rover," *Science*, vol. 343, no. 6169, 2014.

[31] K. Copeland and C. J. Mertens, "Cari-nairas: Calculating flight doses from nairas data using cari," Tech. Rep. DOT/FAA/AM-14/13, Federal Aviation Administration, Office of Aerospace Medicine, Washington, DC, December 2014.

[32] N. A. Schwadron, F. Rahmanifard, J. Wilson, A. P. Jordan, H. E. Spence, C. J. Joyce, J. B. Blake, A. W. Case, W. de Wet, W. M. Farrell, J. C. Kasper, M. D. Looper, N. Lugaz, L. Mays, J. E. Mazur, J. Niehof, N. Petro, C. W. Smith, L. W. Townsend, R. Winslow, and C. Zeitlin, "Update on the worsening particle radiation environment observed by crater and implications for future human deep-space exploration," *Space Weather*, vol. 16, no. 3, pp. 289–303, 2018.

[33] K. Anthony, "Timepix detectors track cosmic radiation on the iss," *CERN News*, 2012.

[34] J. Jakůbek, "semiconductor pixel detectors and their applications in life sciences," *Journal of Instrumentation*, vol. 4, no. 03, pp. P03013,P03013, 2009-03-01.

[35] Medipix. Found at `https://medipix.web.cern.ch/`.

[36] M. Campbell, "10 years of the medipix2 collaboration," *Nuclear Instruments and Methods in Physics Research, A*, vol. 633, 2011-05-01.

[37] M. Kroupa, A. Bahadori, T. Campbell-Ricketts, A. Empl, S. M. Hoang, J. Idarraga-Munoz, R. Rios, E. Semones, N. Stoffle, L. Tlustos, D. Turecek, and L. Pinsky, "A semiconductor radiation imaging pixel detector for space radiation dosimetry," *Life Sciences in Space Research*, vol. 6, pp. 69,78, 2015-07.

[38] J. Uher, C. Fröjdh, T. Holý, J. Jakůbek, S. Petersson, S. Pospíšif, G. Thungström, D. Vavřík, and Z. Vykydal, "Silicon detectors for neutron imaging," *AIP Conference Proceedings*, vol. 958, no. 1, pp. 101–104, 2007.

[39] M. F. Walsh, "first ct using medipix3 and the mars-ct-3 spectral scanner," *Journal of Instrumentation*, vol. 6, no. 01, pp. C01095,C01095, 2011-01-01.

[40] R. Muller, "First 3d colour x-ray of a human using cern technology." News Article, July 2018.

[41] ADVACAM. Found at `https://www.advacam.com`.

[42] D. Turecek and J. Jakubek, "Dependence on temperature and pixel threshold of the calibration for the timepix detector and its correction method," *Journal of Instrumentation*, vol. 7, pp. 1,6, 2013-01-01.

[43] D. Turecek, "small dosimeter based on timepix device for international space station," *Journal of Instrumentation*, vol. 6, no. 12, pp. C12037,C12037, 2011-12-01.

[44] J. Jakubek, "Precise energy calibration of pixel detector working in time-over-threshold mode," *Nuclear Inst. and Methods in Physics Research, A*, vol. 633, no. 1, pp. S262,S266, 2011-05.

[45] J. Bartovsky, D. Schneider, E. Dokladalova, P. Dokladal, V. Georgiev, and M. Akil, "Morphological classification of particles recorded by the timepix detector," in *2011 7th International Symposium on Image and Signal Processing and Analysis (ISPA)*, pp. 343–348, Sep. 2011.

[46] C. Granja, J. Jakubek, S. Polansky, V. Zach, P. Krist, D. Chvatil, J. Stursa, M. Sommer, O. Ploc, S. Kodaira, and M. Martisikova, "Resolving power of pixel detector timepix for wide-range electron, proton and ion detection," *Nuclear Inst. and Methods in Physics Research, A*, vol. 908, no. 11, pp. 60,71, 2018-11-11.

[47] W. Furnell, A. Shenoy, E. Fox, and P. Hatfield, "First results from the lucid-timepix spacecraft payload onboard the techdemosat-1 satellite in low earth orbit," *Advances in Space Research*, vol. 63, no. 5, pp. 1523,1540, 2019-03-01.

[48] J. Jakubek, C. Granja, B. Hartmann, O. Jaekel, M. Martisikova, L. Opalka, and S. Pospisil, "Imaging with secondary radiation in hadron therapy beams with the 3d sensitive voxel detector," in *2011 IEEE Nuclear Science Symposium Conference Record*, pp. 2281,2284, IEEE, 2011-10.

[49] J. Jakubek, "selective detection of secondary particles and neutrons produced in ion beam therapy with 3d sensitive voxel detector," *Journal of Instrumentation*, vol. 6, no. 12, pp. C12010,C12010, 2011-12-01.

[50] K. Akiba, M. Artuso, R. Badman, A. Borgia, R. Bates, F. Bayer, M. van Beuzekom, J. Buytaert, E. Cabruja, M. Campbell, P. Collins, M. Crossley, R. Dumps, L. Eklund, D. Esperante, C. Fleta, A. Gallas, M. Gandelman, J. Garofoli, and M. Gersabeck, "Charged particle tracking with the timepix asic," *Nuclear Inst. and Methods in Physics Research, A*, vol. 661, no. 1, pp. 31,49, 2012.

[51] ICRP, "The 2007 Recommendations of the International Commission on Radiological Protection. ICRP Publication 103," *ICRP*, pp. 1–332, 2007.

[52] F. Cucinotta, M. Kim, and L. Chappell, "Space radiation cancer risk projections and uncertainties – 2010," tech. rep., NASA, 2010.

[53] S. Guatelli, M. Reinhard, B. Mascialino, D. Prokopovich, A. Dzurak, M. Zaider, and A. Rosenfeld, "Tissue equivalence correction in silicon microdosimetry for protons characteristic of the leo space environment," *Nuclear Science, IEEE Transactions on*, vol. 55, pp. 3407 – 3413, 01 2009.

[54] D. Bolst, S. Guatelli, L. T. Tran, L. Chartier, M. L. F. Lerch, N. Matsufuji, and A. B. Rosenfeld, "Correction factors to convert microdosimetry measurements in silicon to tissue in 12 c ion therapy," *Physics in Medicine and Biology*, vol. 62, no. 6, pp. 2055,2069, 2017-03-21.

[55] S. Hoang, L. Pinsky, R. Vilalta, and J. Jakubek, "Let estimation of heavy ion particles based on a timepix-based si detector," *Journal of Physics: Conference Series*, vol. 396, no. 2, p. 8, 2012-12-13.

[56] N. Stoffle, L. Pinsky, M. Kroupa, S. Hoang, J. Idarraga, C. Amberboy, R. Rios, J. Hauss, J. Keller, A. Bahadori, E. Semones, D. Turecek, J. Jakubek, Z. Vykydal, and S. Pospisil, "Timepix-based radiation environment monitor measurements aboard the international space station," *Nuclear Instruments and Methods in Physics Research Section A: Accelerators, Spectrometers, Detectors and Associated Equipment*, vol. 782, pp. 143 – 148, 2015.

[57] High Altitude Student Platform. Found at `https://laspace.lsu.edu/hasp/`.

[58] M. F. Ismail, M. T. H. Sultan, A. Hamdan, and A. U. Md Shah, "A study on the low velocity impact response of hybrid kenaf-kevlar composite laminates through drop test rig technique," *BioResources*, vol. 13, no. 2, pp. 3045–3060, 2018-02-01.

[59] National Aeronautics and Space Administration, "U.S. Standard Atmosphere," Tech. Rep. NASA-TM-X-74335, NOAA-S/T-76-1562, United States of America, 1976.

[60] B. Zábori, A. Hirn, S. Deme, I. Apáthy, A. Csőke, T. Pázmándi, and P. Szántó, "Space dosimetry measurements in the stratosphere using different active and passive dosimetry systems," *Radiation protection dosimetry*, vol. 171, no. 4, pp. 453–462, 2016.

[61] D. T. Phillips, "Intercontinental space weather balloon network," 2016.

[62] E. Ross and W. J. Chaplin, "The behaviour of galactic cosmic-ray intensity during solar activity cycle 24," *Solar physics*, vol. 294, no. 1, p. 8, 2019.

[63] A. Ferrari, P. Sala, A. Fassò, and J. Ranft, "Fluka: a multi-particle transport code." CERN–2005–10 (2005), INFN/TC 05/11, SLAC–R–773.

[64] T. Böhlen, F. Cerutti, M. Chin, A. Fassò, A. Ferrari, P. Ortega, A. Mairani, P. Sala, G. Smirnov, and V. Vlachoudis, "The Fluka code: Developments and challenges for high energy and medical applications." Nuclear Data Sheets 120, 211–214 (2014).

[65] V. Vlachoudis, "FLAIR: A powerful but user friendly graphical interface for FLUKA." Proc. Int. Conf. on Mathematics, Computational Methods & Reactor Physics (M&C 2009), Saratoga Springs, New York, 2009.

[66] M. Pelliccioni, "Protection quantities and conversion coefficients for use in radiation shielding," *Journal of Nuclear Science and Technology*, vol. 37, no. sup1, pp. 850–854, 2000.

[67] G. D. Badhwar and P. O'Neill, "Galactic cosmic radiation model and its applications," *Advances in Space Research*, vol. 17, no. 2, pp. 7–17, 1996.

[68] G. Battistoni, J. Bauer, T. T. Boehlen, F. Cerutti, M. P. Chin, R. Dos Santos Augusto, A. Ferrari, P. G. Ortega, W. Kozłowska, G. Magro, *et al.*, "The fluka code: an accurate simulation tool for particle therapy," *Frontiers in oncology*, vol. 6, p. 116, 2016.

[69] I. Rinaldi, A. Ferrari, A. Mairani, H. Paganetti, K. Parodi, and P. Sala, "An integral test of fluka nuclear models with 160 mev proton beams in multi-layer faraday cups," *Physics in Medicine & Biology*, vol. 56, no. 13, p. 4001, 2011.

[70] A. Fassò and J. Poirier, "Spatial and energy distribution of muons in γ-induced air showers," *Physical Review D*, vol. 63, Dec 2000.

[71] T. Wilson and K. Lee, "Gcr-induced photon luminescence of the moon: The moon as a cr detector," *Proceedings of the 30th International Cosmic Ray Conference, ICRC 2007*, vol. 1, 01 2008.

[72] C. Hagmann, D. Lange, and D. Wright, "Monte carlo simulation of proton-induced cosimc ray cascades in the atmosphere," tech. rep., Lawrence Livermore National Lab.(LLNL), Livermore, CA (United States), 2007.

[73] O. Adriani, G. Barbarino, G. Bazilevskaya, R. Bellotti, M. Boezio, E. Bogomolov, M. Bongi, V. Bonvicini, S. Bottai, A. Bruno, *et al.*, "Pamela's measurements of geomagnetic cutoff variations during the 14 december 2006 storm," *Space Weather*, vol. 14, no. 3, pp. 210–220, 2016.

[74] I. Bacioiu, "Study of the extensive air shower size and the energy spectra of cosmic ray muons at sea level," *Rom. Rep. Phys.*, vol. 66, p. 973, 2014.

[75] C. Patrignani *et al.*, "30.1. primary spectra," *The Review of Particle Physics*, 2017. Available at `http://pdg.lbl.gov/2017/reviews/rpp2017-rev-cosmic-rays.pdf`.

[76] P. Shukla and S. Sankrith, "Energy and angular distributions of atmospheric muons at the earth," *International Journal of Modern Physics A*, vol. 33, no. 30, p. 1850175, 2018.

[77] A. Ferrari, M. Pelliccioni, and R. Villari, "A mathematical model of aircraft for evaluating the effects of shielding structure on aircrew exposure," *Radiation protection dosimetry*, vol. 116, no. 1-4, pp. 331–335, 2005.

[78] S. Nowicki, S. Wender, A. Couture, L. Dominik, A. Warniment, K. McKeown, and M. Mocko, "Thermal neutron flux characterization at aircraft altitudes with the tinman detector," in *2017 IEEE Aerospace Conference*, pp. 1–9, IEEE, 2017.